Chapter 3

A new transformation-free generalized (5,5) compact discretization of transient Navier-Stokes/Boussinesq equations on nonuniform grids

3.1 Introduction

In the preceding chapters we have discussed the advantages and applicability of compact FD schemes along with their historical developments. We have witnessed an overwhelming number of studies concerning compact schemes in the literature. While most of the time-honored compact schemes developed focus on resolving a fluid flow problem on uniform meshes only, significant attention towards utilizing the leverage of nonuniform grids could be seen in recent years. A pioneering attempt on the generalization of implicit compact schemes was carried out by Gamet *et al.* [46] in 1999. Authors of [46] proposed wide stencil discretization of compact methods established by Lele [95] on nonuniform grids. For further development of very high-order compact approximation for first-order and second-order derivative terms on nonuniform grids Shukla and Zhong [142] in 2004 used polynomial interpolation, subsequently employing these approximations to numerically estimate the solution of incompressible N-S equations. Sengupta *et al.* [136] proposed compact discretization of Laplacian operator in self-adjoint form. This study has since been expanded to incorporate a self-adjoint operator approximation in stretched one parameter grids. Recently Sengupta and Sengupta [135] have proposed bi-diagonal compact schemes for nonuniform grids. Later, it was expanded to suggest a hybrid, nonuniform grid-applicable sixth-order spatial discretization [139]. Fan [39] developed the idea of a standard upwind compact scheme adapted to a nonuniform Cartesian grid. On the other hand, Kalita *et al.* [77] in 2004 proposed explicit HOC discretization of steady CDE on nonuniform grids. This HOC approximation was extended to transient N-S equations on nonuniform grids by Kalita *et al.* [78] in 2008. Yu and Tian [175] initiated the discretization of the biharmonic equation on the nonuniform grid in 2013. Authors in this study were able to develop a five-point near second-order accurate method for $\psi - v$ formulation of incompressible N-S equations. A compact discretization of second-order accuracy was recently developed by Kumar and Kalita [86] for the biharmonic formulation of the steady N-S equations on nonuniform grids. All the aforementioned generalizations have invariably expanded the scope and applicability of compact schemes. As such, challenging flow simulations could be carried out with relative ease.

Of late, Sen [130] introduced a novel family of fourth-order implicit compact schemes in which not only the transport variable but also its gradients at surrounding grid points are carried as unknowns. This method was developed for the convection-diffusion problem and was found to carry adequate resolution properties. It combines the advantages of compact discretization and the Padé scheme for spatial derivatives. When compared to other well-known compact approaches, it exhibits lesser dissipation errors. With limited success, the author was able to expand this approach beyond rectangular domains [131]. To fully exploit the advantages of the above methodology, it is crucial to discretize the unsteady Navier-Stokes equations on nonuniform grids without transformation. Such an approximation should be able to handle the extreme clustering needed to capture small flow scales [86] as well as the destabilizing effects of grid stretching [186].

The compact approach is extended in this chapter so as to discretize the N-S equation on a nonuniform grid. This generalization, which might also be referred to as the generalized (5,5)CC approximation, retains the original five-point stencil with constant coefficients. The proposed formulation carries truncation accuracy of order two in both space and time. In the process, it was imperative to induce Padé type approximation on a nonuniform grid. The main novelty here is the development of a constant-coefficient compact scheme on a nonuniform grid, enabling reliable higher-order computations in an extended setup that resolves high gradient flow regions. Further, the formulation continues to combine virtues of compact discretization and Padé approximation on a nonuniform mesh. Methods developed here lead to stable higher-order discretization in conjunction with both Neumann and Dirichlet boundary conditions. The scheme thus developed can be used with ease for both primitive variable (u, v, p) and streamfunction-vorticity $(\psi - \omega)$ form of transient N-S equation in two dimensions. Another popular formulation, the so-called streamfunction-velocity $(\psi - v)$ approach, is not considered in this study because it leads to the discretization of the Biharmonic equation and is not compatible with the prototype second-order partial differential equation used in this study [38, 54, 86, 115, 175]. The numerical problems solved aid in determining the efficacy of the newly designed formulation. The scheme developed helps us focus attention to critical *Re* values known as Hopf's bifurcation points where the transition from a steady flow to time-periodic flow occur. This manifests the utility of the scheme for internal and external flow problems. Additionally, the scheme is tested for temperature gradient-driven flows. To that purpose, we approximate the unsteady Boussinesq equation thereby establishing wider applicability of the discretization procedure.

The rest of the chapter is divided into four sections. In section 3.2, compact discretization of transient N-S equations is developed on the nonuniform grid. We describe the solution procedure of associated algebraic systems in section 3.3. Six numerical tests of varying complexity are addressed in section 3.4. Finally in section 3.5, we summarize our conclusion.

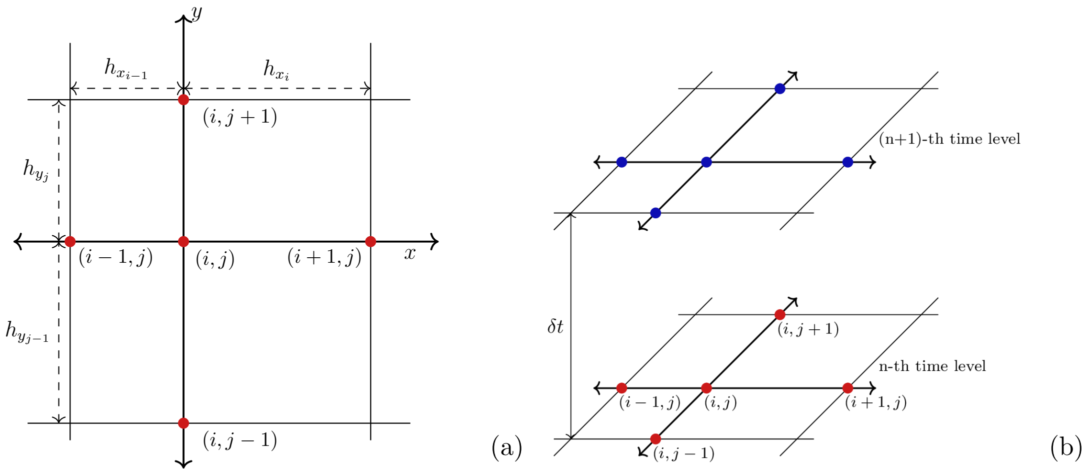

Fig. 3.1: (a) Projection of nonuniform computational stencil in xy plane and (b) Nonuniform computational stencil in xyt hyper-plane.

3.2 Numerical discretization and scheme development

The unsteady 2D incompressible viscous flows governed by the Navier-Stokes equations in the nondimensional primitive variable formulation as well as in $\psi - \omega$ formulation has been presented in equations (1.1) and (1.2). In case of the primitive variable formulation the pressure Poisson equation (PPE)

$$-\nabla^2 p = \left(\frac{\partial u}{\partial x}\right)^2 + 2\frac{\partial u}{\partial y}\frac{\partial v}{\partial x} + \left(\frac{\partial v}{\partial y}\right)^2 \tag{3.1}$$

is used along with the coupled PDEs (1.1a) and (1.1b) to evaluate the pressure field.

In 2D cartesian coordinate system, with appropriate choices of the matrices $\boldsymbol{D}$ and $\boldsymbol{C}$ the CDE (1.4) can be obtained as

$$a\frac{\partial \phi}{\partial t} - \nabla^2 \phi + c_1(x, y, t)\frac{\partial \phi}{\partial x} + c_2(x, y, t)\frac{\partial \phi}{\partial y} = f(x, y, t), (x, y, t) \in \Omega \times (0, T]. \tag{3.2}$$

Here, c_1 and c_2 respectively are convection coefficients in the x- and y-directions, $\Omega = [a_x, b_x] \times [a_y, b_y] \subset \mathbb{R}^2$ is a rectangular domain. The PPE (3.1) is also represented by the steady version of equation (3.2).

In the preceding chapter, we have developed a transformation-free compact discretization strategy for the steady CDE (2.1) on 3D Cartesian nonuniform grids. Here, we shall modify the strategy to address the transient CDE (3.2). The space discretization of equation (3.2) is carried out in the rectangular domain $[a_x, b_x] \times [a_y, b_y]$, where the intervals $[a_x, b_x]$ and $[a_y, b_y]$ are divided into subintervals $a_x = x_1 > x_2 > x_3 > \cdots > x_{n_x} = b_x$ and $a_y = y_1 > y_2 > y_3 > \cdots > y_{n_y} = b_y$ respectively, allowing the subintervals to be unequal whenever necessary. We introduce the mesh spacings along x- and y-direction respectively as

$$\begin{aligned} h_{x_i} &= x_{i+1} - x_i, \quad i \in \{1, 2, 3, \ldots, n_x - 1\}, \\ h_{y_j} &= y_{j+1} - y_j, \quad j \in \{1, 2, 3, \ldots, n_y - 1\}. \end{aligned}$$

Using the compact discretizations of first-order and second-order derivatives in nonuniform grids from equations (2.10) and (2.11) the semidiscrete form of the CDE around the node (i, j) can be found as

$$a \left. \frac{\partial \phi}{\partial t} \right|_{i,j} + [\mathscr{B}\phi]_{i,j} = f_{i,j} \tag{3.3}$$

with the discrete operator $\mathscr{B}$ defined as

$$\begin{aligned} [\mathscr{B}\phi]_{i,j} = &- \left(2B_1\delta_x^2 + 2B_2\delta_y^2 + \frac{B_3}{h_{x_{i-1}}}\delta_x + \frac{B_4}{h_{y_{j-1}}}\delta_y \right) \phi_{i,j} \\ &+ \left(B_1\delta_x + \frac{B_3}{h_{x_{i-1}}} + c_1 \right) \phi_{x_{i,j}} + \left(B_2\delta_y + \frac{B_4}{h_{y_{j-1}}} + c_2 \right) \phi_{y_{i,j}} \end{aligned} \tag{3.4}$$

where,

$$B_1 = \frac{2(1 - \alpha_x + \alpha_x^2)}{(1 + \alpha_x^2)}, B_2 = \frac{2(1 - \alpha_y + \alpha_y^2)}{(1 + \alpha_y^2)}, B_3 = \frac{2(1 - \alpha_x)}{(1 + \alpha_x^2)}, B_4 = \frac{2(1 - \alpha_y)}{(1 + \alpha_y^2)}.$$

Grid spacing varies with node in the case of nonuniform mesh grids, so do the values of B_1, B_2, B_3, and B_4. It is worth noting that given a uniform grid, they remain fixed because α_x and α_y remain constant throughout. It is to be noted that difference operator $\mathscr{B}$ carries gradients of the flow variables. These gradients are needed to be estimated up to the desired order of accuracy. On a uniform grid, this was rather straightforward and could be accomplished using Padé approximations [95]. We generalize the idea and appear at the following approximations for spatial derivatives of third-order accuracy on the nonuniform grid, which co-relates to fourth-order accuracy of the original Padé approximation on a uniform grid.

$$\left(1+\frac{h_{x_i}h_{x_{i-1}}}{6}\delta_x^2\right)\phi_{x_{i,j}} = \left(\delta_x - \frac{h_{x_i}-h_{x_{i-1}}}{2}\delta_x^2\right)\phi_{i,j} + \mathscr{O}\left((h_{x_i}-h_{x_{i-1}})(3h_{x_i}^2+h_{x_i}h_{x_{i-1}}+3h_{x_{i-1}}^2)\right) \tag{3.5}$$

and

$$\left(1+\frac{h_{y_j}h_{y_{j-1}}}{6}\delta_y^2\right)\phi_{y_{i,j}} = \left(\delta_y - \frac{h_{y_j}-h_{y_{j-1}}}{2}\delta_y^2\right)\phi_{i,j} + \mathscr{O}\left((h_{y_j}-h_{y_{j-1}})(3h_{y_j}^2+h_{y_j}h_{y_{j-1}}+3h_{y_{j-1}}^2)\right). \tag{3.6}$$

Finally, for the temporal discretization of the unsteady term in equation (3.2), we adopt the Crank-Nicholson approximation. Thus, the fully discretized form of the unsteady CDE on a nonuniform grid is

$$\left(1+\frac{\delta t}{2a}\mathscr{B}\right)\phi_{i,j}^{n+1} = \left(1-\frac{\delta t}{2a}\mathscr{B}\right)\phi_{i,j}^{n} + \frac{\delta t}{2a}\left(f_{i,j}^{n+1}+f_{i,j}^{n}\right). \tag{3.7}$$

Above is a compact formulation capable of handling nonuniform grids. It can directly be employed on the physical plane thereby avoiding inherent difficulties associated with coordinate transformation. According to truncation error, this novel approach has a point-wise spatial accuracy of at least two. On uniform grid, the accuracy is seen to be reverted to four [77, 78].

As we are going to deal with N-S equations in their primitive variable form, where pressure usually needed to be calculated from pressure gradients, it's also vital that we introduce one-sided approximations of first-order derivatives. Additionally, because flow gradients are variables in the present scheme, it is important to estimate gradients at boundary points in the case of the nonprimitive formulation. This is accomplished by introducing the following estimates.

On the left boundary, $\forall 1 \le j \le n_y$:

$$\phi_{x_{1,j}} = -\frac{h_{x_1}}{h_{x_2}(h_{x_1}+h_{x_2})}\phi_{3,j} + \frac{h_{x_1}+h_{x_2}}{h_{x_1}h_{x_2}}\phi_{2,j} - \frac{2h_{x_1}+h_{x_2}}{h_{x_1}(h_{x_1}+h_{x_2})}\phi_{1,j} + \mathscr{O}\left(h_{x_1}(h_{x_1}+h_{x_2})\right). \tag{3.8}$$

On the bottom boundary, $\forall 1 \le i \le n_x$:

$$\phi_{y_{i,1}} = -\frac{h_{y_1}}{h_{y_2}(h_{y_1}+h_{y_2})}\phi_{i,3} + \frac{h_{y_1}+h_{y_2}}{h_{y_1}h_{y_2}}\phi_{i,2} - \frac{2h_{y_1}+h_{y_2}}{h_{y_1}(h_{y_1}+h_{y_2})}\phi_{i,1} + \mathscr{O}\left(h_{y_1}(h_{y_1}+h_{y_2})\right). \tag{3.9}$$

On the right boundary, $\forall 1 \leq j \leq n_y$:

$$\begin{aligned}\phi_{x_{n_x,j}} =& \frac{h_{x_{n_x-1}}}{h_{x_{n_x-2}}(h_{x_{n_x-1}}+h_{x_{n_x-2}})}\phi_{n_x-2,j} - \frac{h_{x_{n_x-1}}+h_{x_{n_x-2}}}{h_{x_{n_x-1}}h_{x_{n_x-2}}}\phi_{n_x-1,j} \\ &+ \frac{2h_{x_{n_x-1}}+h_{x_{n_x-2}}}{h_{x_{n_x-1}}(h_{x_{n_x-1}}+h_{x_{n_x-2}})}\phi_{n_x,j} + \mathcal{O}\left(h_{x_{n_x-2}}(h_{x_{n_x-1}}+h_{x_{n_x-2}})\right).\end{aligned} \tag{3.10}$$

On the top boundary, $\forall 1 \leq i \leq n_x$:

$$\begin{aligned}\phi_{y_{i,n_y}} =& \frac{h_{y_{n_y-1}}}{h_{y_{n_y-2}}(h_{y_{n_y-1}}+h_{y_{n_y-2}})}\phi_{i,n_y-2} - \frac{h_{y_{n_y-1}}+h_{y_{n_y-2}}}{h_{y_{n_y-1}}h_{y_{n_y-2}}}\phi_{i,n_y-1} \\ &+ \frac{2h_{y_{n_y-1}}+h_{y_{n_y-2}}}{h_{y_{n_y-1}}(h_{y_{n_y-1}}+h_{y_{n_y-2}})}\phi_{i,n_y} + \mathcal{O}\left(h_{y_{n_y-2}}(h_{y_{n_y-1}}+h_{y_{n_y-2}})\right).\end{aligned} \tag{3.11}$$

In the next section, we shall briefly discuss the solution techniques required to solve the system of equations resulting from the above discretization. Competency of the methodology on different kinds of nonuniform grids in conjunction with various flow problems will be reported in section 3.4.

3.3 Solution of associated systems of equations

As we desire to time march from nth to $(n+1)$th level, the algebraic system associated with the newly developed scheme presented in equation (3.7) at (i,j)th node might be written in expanded form as

$$\begin{aligned}&(a+\widehat{B}_1)\phi_{i,j}^{n+1} - \widehat{B}_2\phi_{i+1,j}^{n+1} - \widehat{B}_3\phi_{i-1,j}^{n+1} - \widehat{B}_4\phi_{i,j+1}^{n+1} - \widehat{B}_5\phi_{i,j-1}^{n+1} \\ &+ \widehat{B}_6\left(\phi_{x_{i+1,j}}^{n+1} - \phi_{x_{i-1,j}}^{n+1}\right) + \left(\widehat{B}_7 + \frac{\delta t}{2}c_1\right)\phi_{x_{i,j}}^{n+1} \\ &+ \widehat{B}_8\left(\phi_{y_{i,j+1}}^{n+1} - \phi_{y_{i,j-1}}^{n+1}\right) + \left(\widehat{B}_9 + \frac{\delta t}{2}c_2\right)\phi_{y_{i,j}}^{n+1} \\ &= (a-\widehat{B}_1)\phi_{i,j}^{n} + \widehat{B}_2\phi_{i+1,j}^{n} + \widehat{B}_3\phi_{i-1,j}^{n} + \widehat{B}_4\phi_{i,j+1}^{n} + \widehat{B}_5\phi_{i,j-1}^{n} \\ &- \widehat{B}_6\left(\phi_{x_{i+1,j}}^{n} - \phi_{x_{i-1,j}}^{n}\right) - \left(\widehat{B}_7 + \frac{\delta t}{2}c_1\right)\phi_{x_{i,j}}^{n} \\ &- \widehat{B}_8\left(\phi_{y_{i,j+1}}^{n} - \phi_{y_{i,j-1}}^{n}\right) - \left(\widehat{B}_9 + \frac{\delta t}{2}c_2\right)\phi_{y_{i,j}}^{n} + \frac{\delta t}{2a}\left(f_{i,j}^{n+1} + f_{i,j}^{n}\right).\end{aligned} \tag{3.12}$$

Similarly, expanded form of approximations given in equations (3.5) and (3.6) are

$$\phi_{x_{i+1,j}}^{n+1} + 2\left(1+\alpha_x\right)\phi_{x_{i,j}}^{n+1} + \alpha_x\phi_{x_{i-1,j}}^{n+1} = \frac{3}{\alpha_x h_{x_{i-1}}}\left(\phi_{i+1,j}^{n+1} - (1-\alpha_x^2)\phi_{i,j}^{n+1} - \alpha_x^2\phi_{i-1,j}^{n+1}\right)$$

(3.13)

and

$$\phi^{n+1}_{y_{i,j+1}} + 2\left(1+\alpha_y\right)\phi^{n+1}_{y_{i,j}} + \alpha_y\phi^{n+1}_{y_{i,j-1}} = \frac{3}{\alpha_y h_{y_{j-1}}}\left(\phi^{n+1}_{i,j+1} - (1-\alpha_y^2)\phi^{n+1}_{i,j} - \alpha_y^2\phi^{n+1}_{i,j-1}\right) \tag{3.14}$$

respectively. The coefficients appearing in equation (3.12) are given below:

$$\begin{aligned}
\widehat{B}_1 &= 2\delta t\left(\frac{B_1}{\alpha_x h^2_{x_{i-1}}} + \frac{B_2}{\alpha_y h^2_{y_{j-1}}}\right), & & \\
\widehat{B}_2 &= \frac{\delta t}{2}\frac{1}{(1+\alpha_x)h^2_{x_{i-1}}}\left(\frac{4B_1}{\alpha_x} + B_3\right), & \widehat{B}_3 &= \frac{\delta t}{2}\frac{1}{(1+\alpha_x)h^2_{x_{i-1}}}\left(4B_1 - B_3\right), \\
\widehat{B}_4 &= \frac{\delta t}{2}\frac{1}{(1+\alpha_y)h^2_{y_{j-1}}}\left(\frac{4B_2}{\alpha_y} + B_4\right), & \widehat{B}_5 &= \frac{\delta t}{2}\frac{1}{(1+\alpha_y)h_{y^2_{j-1}}}\left(4B_2 - B_4\right), \\
\widehat{B}_6 &= \frac{\delta t}{2}\frac{B_1}{(1+\alpha_x)h_{x_{i-1}}}, & \widehat{B}_7 &= \frac{\delta t}{2}\frac{B_3}{h_{x_{i-1}}}, \\
\widehat{B}_8 &= \frac{\delta t}{2}\frac{B_2}{(1+\alpha_y)h_{y_{j-1}}}, & \widehat{B}_9 &= \frac{\delta t}{2}\frac{B_3}{h_{y_{j-1}}}.
\end{aligned}$$

Here, $\widehat{B}_i$'s, for $i \in \{1, 2, \ldots, 9\}$, solely depend on the grid spacings and remain invariant once the grid is set up. Therefore, for a system with constant convection and diffusion coefficients, the newly developed discretization offers the benefit of solving the resulting system of equations with constant coefficients. This is an inherent advantage of this formulation over other compact formulations that have been proposed in the literature [70, 77, 78, 86, 115, 117, 118, 142, 157, 175]. Thus on a grid of size $n_x \times n_y$, one is required to solve a system with a constant coefficient matrix. Although it appears that the system has a large dimension $3n_xn_y \times 3n_xn_y$, but following a predictor-corrector approach as discussed in [130, 134] one neeeds to deal with a system of size $n_x \times n_y$ only. For completeness, the key steps in the procedure are given below.

The finite difference approximation (3.12), when written at each grid point can be put in the form

$$M_1\Phi^{(n+1)} = F_1\left(\Phi^{(n)}, \Phi^{(n)}_x, \Phi^{(n)}_y, \Phi^{(n+1)}_x, \Phi^{(n+1)}_y\right) \tag{3.15}$$

with

$$\Phi \;=\; \left(\phi_{1,1}, \phi_{1,2}, \ldots, \phi_{1,n_y}, \phi_{2,1}, \phi_{2,2}, \ldots, \phi_{2,n_y}, \ldots, \phi_{n_x,n_y}\right)^T,$$

$$\begin{aligned} \Phi_x &= \left(\phi_{x_{1,1}}, \phi_{x_{1,2}}, \ldots, \phi_{x_{1,n_y}}, \phi_{x_{2,1}}, \phi_{x_{2,2}}, \ldots, \phi_{x_{2,n_y}}, \ldots, \phi_{x_{n_x,n_y}}\right)^T \\ \text{and} \quad \Phi_y &= \left(\phi_{y_{1,1}}, \phi_{y_{1,2}}, \ldots, \phi_{y_{1,n_y}}, \phi_{y_{2,1}}, \phi_{y_{2,2}}, \ldots, \phi_{y_{2,n_y}}, \ldots, \phi_{y_{n_x,n_y}}\right)^T. \end{aligned}$$

The coefficient matrix M_1 is a sparse nonsymmetric matrix of dimension $n_x n_y$ with five nonzero diagonals. Similarly matrix representation of equation (3.13) and equation (3.14) are

$$M_2 \Phi_x^{(n)} = F_2\left(\Phi^{(n)}\right) \tag{3.16}$$

and

$$M_3 \Phi_y^{(n)} = F_3\left(\Phi^{(n)}\right) \tag{3.17}$$

respectively. M_2 and M_3 are tri-diagonal matrices and hence systems (3.16) and (3.17) are very amenable to efficient computation. The algorithmic procedure adopted at this stage is same as delineated in [130, 134].

3.4 Numerical examples

To examine the accuracy and effectiveness of the scheme developed, it has been applied to six different problems of varying complexity. Verification study is carried out using three problems *viz.* convection and diffusion of Gaussian pulse, Boussinesq equation with an analytical solution and flow decayed by viscosity where the primitive variable formulation is used. Subsequently, we validate our newly developed method by solving the lid-driven square cavity problem and simulating a flow field past a square cylinder. Finally, the natural heat convection in a square cavity is simulated. The intention behind selecting these problems is to highlight the inherent flexibility of nonuniform grids whereby certain portions of the solution domain can be better resolved with grid clustering. Furthermore, the abundance of numerical solutions gives us the leverage to compare our numerical solution with the existing ones. For the viscous flow of driven cavity and past the bluff body our emphasis is on transitional *Re* values which characterize transitional instability.

3.4.1 Problem 1: Convection and diffusion of Gaussian pulse

The first numerical example handles unsteady convection-diffusion of a Gaussian pulse in the square $[0,2] \times [0,2]$. The analytical solution of the problem is given by

$$\phi(x,y,t) = \frac{1}{4t+1} \exp\left[-\frac{(ax-c_1t-0.5a)^2}{a(4t+1)} - \frac{(ax-c_2t-0.5a)^2}{a(4t+1)}\right]. \tag{3.18}$$

The initial condition and Dirichlet boundary conditions are directly supplied by equation (3.18). At $t=0$, equation (3.18) represents a pulse of unit height centred at $(0.5, 0.5)$.

For this exercise, two distinct mathematical situations with contrasting convection coefficient combinations $c_1 = c_2 = 150$ and $c_1 = c_2 = 50$ have been taken into consideration. For both the situations, that values $a = 100$ and $\delta t = 2.5e-5$ are kept constant. A nonuniform grid that stretches geometrically in both the x- and y-directions is set up for the first scenario. The grid is generated using equation (2.27). Fig. 3.2a displays one such example of a grid thus formed. Following the work of Sengupta and Sengupta [135] nonuniform grids of sizes 91×91, 121×121 and 161×161 are generated with $\alpha_x = \alpha_y = 1.001$ and the appropriate choices of initial spacings X_0 and Y_0. In order to prevent a rapid exponential increase in grid spacing produced by greater values of these ratios, we must deal with values of α_x and α_y that are close to unity [135]. For the second instance, a different nonuniform grid is constructed using the trigonometric function provided in equation (2.28). For this scenario, the clustering parameters λ_x and λ_y are both kept at 0.6. For additional constants $L_x = L_y = 2$ and $\Theta_x = \Theta_y = 4\pi$ have been taken.

In Fig. 3.3a and 3.3b the contour of exact and numerically approximated pulses are displayed at time $t = 0.25$ and 0.50 respectively. Comparisons between the exact and computed solutions at time $t = 1.0$ and 1.5 are depicted in Fig. 3.3c and 3.3d respectively. We can see from the figures that the present scheme is flawless in capturing the moving pulse with very high accuracy and the numerical solution is almost identical to the exact one.

A qualitative comparison of the spatial accuracy of present scheme is computed in Table 3.1. In this table, we have also calculated the numerical rate of convergence

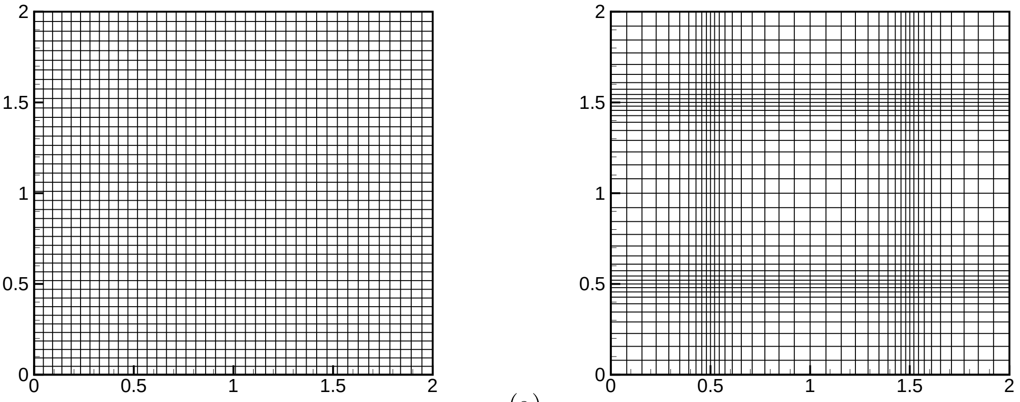

(a) (b)

Fig. 3.2: Problem 1: Typical 161×161 nonuniform grids : (a) geometric stretching and (b) centrosymetric variation (only every fourth gridline along each direction are shown).

Table 3.1: Problem 1: L_1, L_2 and L_∞-norm errors of ϕ at different grids and spatial rate of convergence along with relative CPU time.

Time	Grid size	91×91	order	121×121	order	161×161
Geometric grid with $a = 100$, $c_1 = c_2 = 150$.						
0.25	L_1	3.223229e-6	4.09	9.925681e-7	4.07	3.077013e-7
	L_2	1.705195e-5	4.10	5.242244e-6	4.08	1.619978e-6
	L_∞	2.463644e-4	4.06	7.668743e-5	4.04	2.399216e-5
CPU time		1		1.66		3.28
0.50	L_1	2.316761e-6	4.08	7.158958e-7	4.02	2.253200e-7
	L_2	1.019866e-5	4.90	3.144176e-6	4.00	9.947138e-7
	L_∞	1.256842e-4	4.15	3.804455e-5	3.86	1.260057e-5
CPU time		2.37		3.63		6.19
Trigonometric grid with $a = 100$, $c_1 = c_2 = 50$.						
1.00	L_1	7.466867e-7	3.76	2.535159e-7	4.35	7.260102e-8
	L_2	3.072387e-6	3.99	9.745576e-7	4.10	2.994137e-7
	L_∞	5.209459e-5	3.96	1.667531e-5	3.83	5.536425e-6
CPU time		1		2.66		5.39
1.50	L_1	8.741302e-7	2.61	4.131198e-7	5.33	8.919653e-8
	L_2	2.533363e-6	3.42	9.459405e-7	4.52	2.578045e-7
	L_∞	2.616313e-5	4.07	8.118162e-6	3.74	2.767202e-6
CPU time		1.48		3.77		8.24

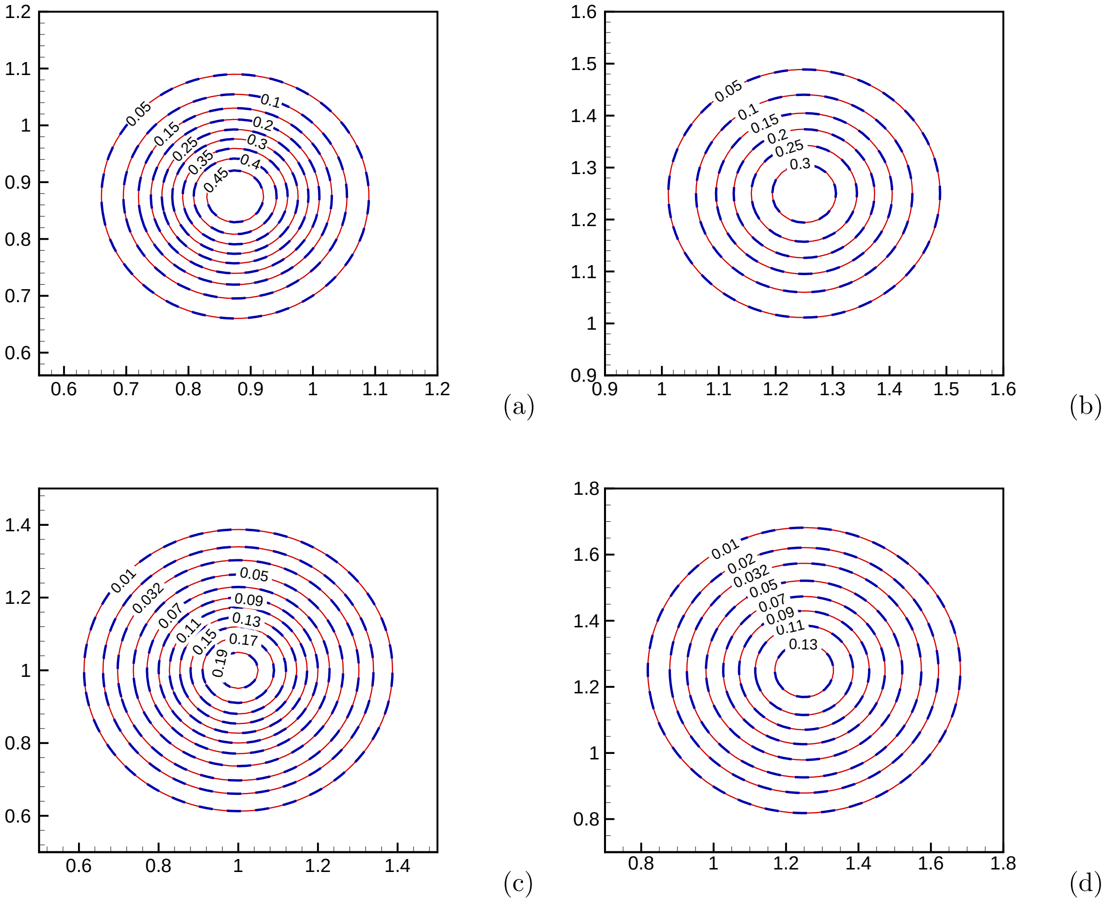

Fig. 3.3: Problem 1: Numerical (blue) and analytical (red) contour plots of the Gaussian pulse at (a) $t = 0.25$, (b) $t = 0.50$ for $a = 100$, $c_1 = c_2 = 150$ and at (c) $t = 1.0$, (d) $t = 1.5$ for $a = 100$, $c_1 = c_2 = 50$.

for computations carried out using both the grids. It is heartening to note that the scheme developed reports nearly fourth-order accuracy in all three norms L_1, L_2 and L_∞. This is consistent with the scheme seeking to recuperate its order of accuracy on a uniform grid. To provide an idea of the increase in computational cost with grid we present relative CPU time in Table 3.1. Linear growth of CPU time could be noticed with increased grid size. Note that the relative time to converge on moving to the finer grid is more in the trigonometric mesh as it leads to extreme stretching. For the temporal order of convergence computations are carried out with $\delta t = 0.02$, 0.01 and 0.005 on two different nonuniform grids of size 121×121. For geometric grid earlier choice of $\alpha_x = \alpha_y = 1.001$ is used whereas for trigonometrically generated grid $\lambda_x = \lambda_y = 0.1$ is adopted. The choice of the grid is such that spatial error is

Table 3.2: Problem 1: L_1, L_2 and L_∞-norm errors of ϕ for different time spacing and temporal order of convergence.

Time		$\delta t = 0.02$	order	$\delta t = 0.01$	order	$\delta t = 0.005$
Geometric grid with $a = 100$, $c_1 = c_2 = 150$ and $Pe = 2.65$.						
0.20	L_1	8.867685e-4	1.96	2.283820e-4	1.99	5.747402e-5
	L_2	4.771255e-3	1.96	1.225416e-3	1.99	3.095043e-4
	L_∞	4.365765e-6	2.03	1.068483e-6	2.01	2.660172e-7
0.50	L_1	9.970811e-4	1.99	2.512729e-4	2.00	6.292680e-5
	L_2	4.266994e-3	1.99	1.073578e-3	2.00	2.688388e-4
	L_∞	3.110319e-6	2.06	7.440859e-7	2.02	1.828845e-7
Trigonometric grid with $a = 100$, $c_1 = c_2 = 50$ and $Pe = 0.92$.						
0.20	L_1	4.273296e-5	2.00	1.066857e-5	2.01	2.651160e-6
	L_2	2.203481e-4	2.00	5.515270e-5	1.98	1.397072e-5
	L_∞	2.702573e-3	2.01	6.727731e-4	1.97	1.712231e-4
0.50	L_1	4.119717e-5	2.00	1.027137e-5	2.01	2.555920e-6
	L_2	1.732644e-4	2.00	4.331754e-5	1.98	1.097946e-5
	L_∞	1.749892e-3	2.00	4.370015e-4	1.96	1.126015e-4

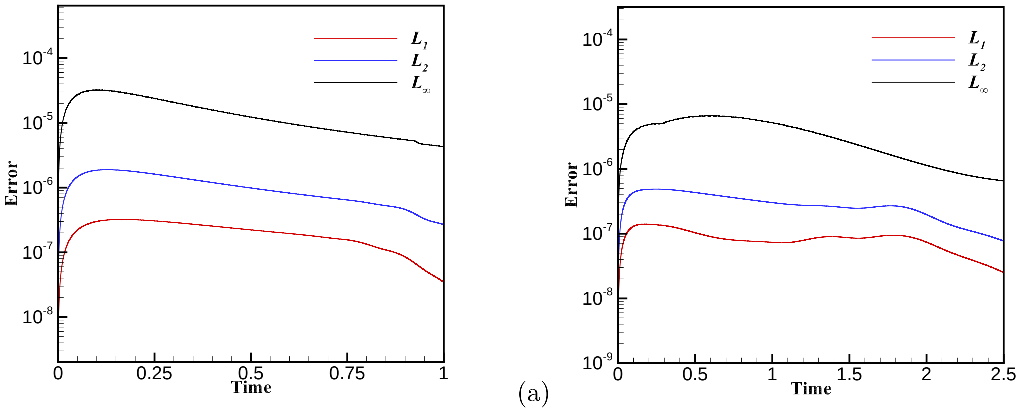

(a) (b)

Fig. 3.4: Problem 1: Time evolution of L_1, L_2 and L_∞-norm errors for $a = 100$, $\delta t = 2.5e-5$ (a) $c_1 = c_2 = 150$, $Pe = 2$ and (b) $c_1 = c_2 = 50$, $Pe = 1$.

much smaller compared to temporal error for all three time steps. Computed errors are compiled in Table 3.2. The temporal rate of convergence close to two can be seen in the table for all cases.

L_1, L_2 and L_∞-norm errors for both the combinations are plotted for the entire simulation at each time step in Fig. 3.4. They validate the similar temporal decaying nature of the errors for all the three norms justifying the convergence of the proposed scheme. The converging criteria for all the outer and inner iterations are set to be $1.0e-10$.

3.4.2 Problem 2: Boussinesq equation with an analytical solution

We extend the verification study by numerically solving the steady form of Boussinesq equation (1.3), in a unit square domain $[0,1]\times[0,1]$, which in nondimensional form is written as

$$\begin{cases} \nabla^2\omega = \dfrac{1}{Pr}\mathbf{u}\cdot\nabla\omega + Ra\dfrac{\partial\mathscr{T}}{\partial x} + f, & (3.19a) \\ \nabla^2\psi = -\omega, & (3.19b) \\ \nabla^2\mathscr{T} = \mathbf{u}\cdot\nabla\mathscr{T}. & (3.19c) \end{cases}$$

It is straightforward to generalize our formulation for the convection-diffusion equation to the Boussinesq equation where three simultaneous equations are to be tackled. The main emphasis here is to document the convergence behavior of the newly developed spatial discretization. We thus work with analytical solution

$$\psi(x,y) = e^{x+y}/Pr, \quad \mathscr{T}(x,y) = x+y \quad \text{and} \quad \omega(x,y) = -2e^{x+y}/Pr$$

along with Dirichlet boundary conditions. The corresponding forcing function could be adequately chosen following works available in the literature [157, 185].

The study has been carried out for $Pr = 10$ and $Ra = 10^4$ on two different nonuniform grids similar to Problem 1. The first one is a slightly stretched geometric grid with α_x and α_y are set to 1.001. Another nonuniform grid has been generated using $\lambda_x = \lambda_y = -0.6$, $L_x = L_y = 1$ and $\Theta_x = \Theta_y = 2\pi$ in the trigonometric grid generating function (2.28). The convergence histories on both grids have been depicted in Fig. 3.5. Steady gradual convergence with some oscillations could be noticed in both cases. Further, the numerical performance of the scheme has been compiled in Table 3.3. Table 3.3 shows L_2 error of ψ, ω and $\mathscr{T}$ at three different grids 17×17, 33×33 and 65×65. The numerical convergence order for this steady

Boussinesq equation is seen to follow the theoretical order of convergence. We also present the relative CPU time of the scheme for different grids in Table 3.3. It is to be noted that with Pr and Ra kept fixed the CPU time increases by a factor five as grid points augment by a factor of four.

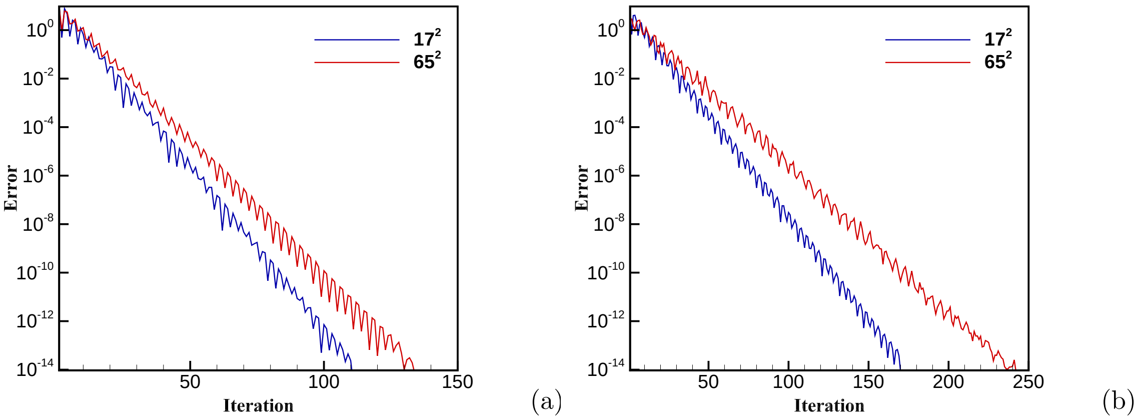

Fig. 3.5: Problem 2: Convergence history showing maximum absolute error of ψ vs iterations numbers on (a) geometrically stretched grid with $\alpha_x = \alpha_y = 1.001$ and (b) trigonometrically scattered grids with $\lambda_x = \lambda_y = -0.6$.

Table 3.3: Problem 2: L_2-norm errors for ψ, ω and $\mathscr{T}$ with relative CPU time for different grid sizes.

	17×17	order	33×33	order	65×65
			Geometric grid with $\alpha_x = \alpha_y = 1.001$.		
ψ	2.021816e-10	4.74	7.587130e-12	2.96	9.784105e-13
ω	1.544622e-8	3.77	1.130076e-9	3.59	9.378200e-11
$\mathscr{T}$	1.728034e-11	3.88	1.170360e-12	3.24	1.240812e-13
CPU time	1.0		5.0		23.6
			Trigonometric grid with $\lambda_x = \lambda_y = -0.6$.		
ψ	4.549466e-8	3.94	2.961104e-9	3.98	1.874735e-10
ω	3.378556e-6	3.98	2.146959e-7	3.98	1.351673e-8
$\mathscr{T}$	4.368400e-9	3.98	2.767796e-10	3.99	1.741595e-11
CPU time	1.8		8.5		42.7

3.4.3 Problem 3: Flow decayed by viscosity

Equation (1.1) governs the flow decayed by viscosity problem [70, 117] in the square region $(x, y) \in [0, \pi] \times [0, \pi]$. The initial conditions of the problem are given by

$$u(x, y, 0) = -\cos(x)\sin(y) \quad \text{and} \quad v(x, y, 0) = \sin(x)\cos(y). \tag{3.20}$$

Here, u and v are the components of $\mathbf{u}$ in x- and y-direction. The exact solution of this problem is

$$\begin{aligned} u(x, y, t) &= -\cos(x)\sin(y)e^{(-2t/Re)}, \\ v(x, y, t) &= \sin(x)\cos(y)e^{(-2t/Re)}, \\ p(x, y, t) &= -\frac{1}{4}\left\{\cos(2x) + \cos(2y)\right\}e^{(-4t/Re)}. \end{aligned} \tag{3.21}$$

Equation (3.21) can be utilized to determine the boundary values of u and v at $x = 0$, $x = \pi$, $y = 0$ and $y = \pi$. After obtaining the solution for u and v using the discretized form of equation (1.1b), their gradients are subsequently obtained from equations (3.5) and (3.6).

We discretize the primitive variable formulation of N-S equation (1.1) for this problem. Traditionally this formulation lacks pressure boundary conditions, thus we work with pressure gradients p_x and p_y rather than actual pressure conditions on the boundary. These pressure gradients are obtained from N-S equations applied to boundary points. Since p, p_x, and p_y are used in the discretization of PPE (3.1), the solution field inevitably includes pressure gradients computed with the help of equations (3.5) and (3.6). Thus no additional computation is necessary for estimating p_x and p_y. The boundary values of p are then updated in each temporal step using the one-sided approximations stated in equations (3.8)–(3.11).

Using $\lambda_x = \lambda_y = 0.6$, $L_x = L_y = \pi$, and $\Theta_x = \Theta_y = 4\pi$ in the function (2.28), a 65×65 centrosymmetric nonuniform grid has been generated. In Fig. 3.6, surface plots and contour plots of the velocities u, v, and pressure p at times $t = 1$ and 15 for $Re = 100$ are displayed alongside. The decaying nature of the flow with viscosity becomes evident from the surface plots. The accuracy of the current scheme is ascertained by the contour plots of the exact and computed values of u, v, and p at

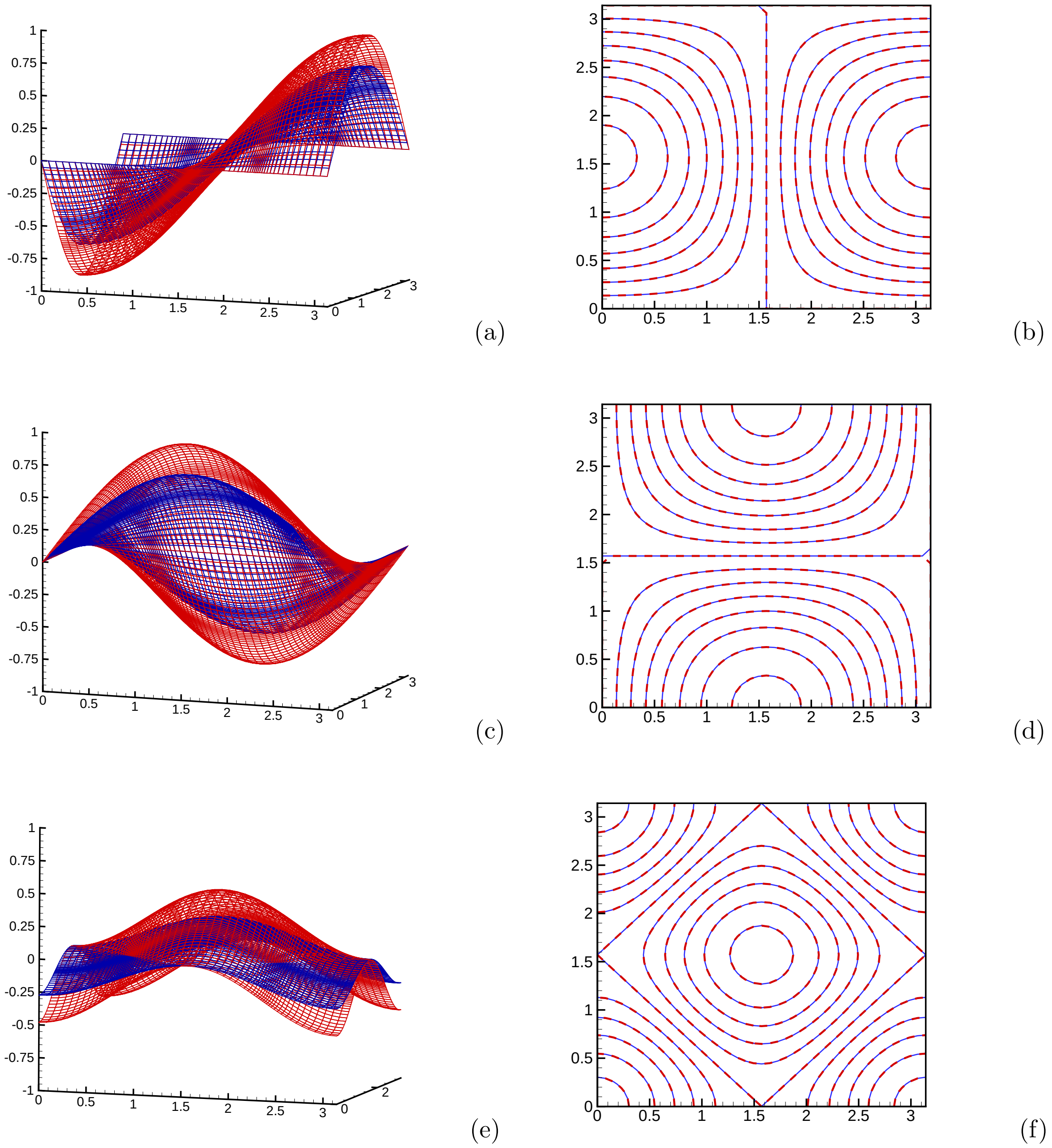

Fig. 3.6: Problem 3: Surface plots at $t = 1$ (red) and $t = 15$ (blue) for (a) u, (c) v, (e) p and numerical (red) and exact (blue) contours plots at $t = 15$ for (b) u, (d) v, (f) p.

time $t = 15$. Tolerance for all inner and outer iterations are set to be $\epsilon = 1.0e - 10$.

Similar to the previous problem, here also we compute using three different grids 17×17, 33×33, and 65×65 to determine the numerical order of convergence. In Table 3.4 we present errors in L_2-norm for u, v and p at time $t = 1$ and 15. At both times the scheme returns good order of accuracy for horizontal and vertical velocities. With the increase in grid size, a gradual reduction of accuracy order

Table 3.4: Problem 3: L_2-norm errors for u, v and p for different grid sizes along with relative CPU time.

Time		17×17	order	33×33	order	65×65
1	u	9.260973e-4	4.03	5.670194e-5	4.74	2.125714e-6
	v	6.915589e-4	3.92	4.558980e-5	3.87	3.117723e-6
	p	6.342758e-4	4.18	3.511948e-5	2.30	7.130818e-6
CPU time		1		10.98		126.37
15	u	2.548289e-3	4.35	1.247658e-4	4.39	5.960460e-6
	v	1.297523e-3	4.10	7.574251e-5	4.13	4.336838e-6
	p	8.975710e-4	4.55	3.834936e-5	2.21	8.265992e-6
CPU time		11.53		146.38		1459.47

can be noticed for pressure. For this and other solutions of the N-S equations, the temporal accuracy of the scheme could be hardly captured as each time step involves several inner iterations due to the nonlinear nature of the equation. Further, spatial error is required to be kept low by taking $\max_i\{h_{x_i}\}$ and $\max_j\{h_{y_j}\}$ very small compared to δt which in turn substantially increases the condition number of the system and is often avoided [130, 134, 185]. From Table 3.4, it is amply clear that with grid points increased from $N \times N$ to $2N \times 2N$ the CPU time augmented by a factor of almost eleven. This is primarily attributed to increased CPU time in solving the pressure Poisson equation whose underlying matrix system is now $4N^2 \times 4N^2$ up from $N^2 \times N^2$.

3.4.4 Problem 4: Lid-driven square cavity

The classical problem of a 2D lid-driven cavity is then addressed using the solution strategy. The movement of fluid inside a lid-driven cavity creates a benchmark situation which has been used extensively in the literature to validate different schemes that has been developed to tackle the Navier-Stokes equations. The simple geometry of the problem shown in Fig. 3.7a makes the application of no-slip boundary conditions relatively easy. At the same time, it is quite challenging to capture vortices of various shapes and sizes accurately i.e. to correctly estimate the position and strength of the vortices formed inside the cavity. Further, being a prominent problem it is possible to find numerous studies on the lid-driven cavity problem in the literature [52, 54, 63, 86, 130, 163, 173]. However, the first change from a steady to a periodic state of the flow inside the cavity occurs at a point known as the Hopf bifurcation point. Although there are some disagreements on the precise Re value at which this transition takes place but Bruneau and Saad [14] using a very fine mesh were able to establish a periodic state of flow at $Re = 8050$.

In this work, to simulate flow inside the cavity defined as the unit square region $[0, 1] \times [0, 1]$ bounded by solid walls, we adopt streamfunction-vorticity formulation of N-S equations given in equation (1.2). The fluid flow inside the cavity is caused by the top wall of the cavity moving on its plane at a uniform speed $u = 1$ from left to right. Other walls of the cavity remain stationary throughout the simulation. From this, the boundary conditions of velocities are extracted as $u = 1$, $v = 0$ at the moving boundary, and $u = 0$, $v = 0$ at the stationary boundaries. We have set the streamfunction values to be zero on all the boundaries. The Neumann boundary conditions for the vorticity that are derived from equation (1.2b) and no-slip condition between the cavity walls and the fluid inside are given below.

On the left wall, $\forall 1 \leq j \leq n_y$:

$$\omega_{1,j} = -\frac{2\psi_{2,j}}{h_{x_1}^2}. \tag{3.22}$$

On the bottom boundary, $\forall 1 \leq i \leq n_x$:

$$\omega_{i,1} = -\frac{2\psi_{i,2}}{h_{y_1}^2}. \tag{3.23}$$

On the right boundary, $\forall 1 \leq j \leq n_y$:

$$\omega_{n_x,j} = -\frac{2\psi_{n_x-1,j}}{h_{x_{n_x-1}}^2}. \tag{3.24}$$

On the top boundary, $\forall 1 \leq i \leq n_x$:

$$\omega_{i,n_y} = -\frac{2(\psi_{i,n_y-1} + h_{y_{n_y-1}})}{h_{y_{n_y-1}}^2}. \tag{3.25}$$

Once the values of vorticity are computed, the boundary values for its gradients are calculated using equations (3.8)–(3.11).

As the vortices are created at solid boundaries and are convected to the interior of the domain, it is crucial to cluster grids in the near boundary region. Further, in the vicinity of the top wall the velocity gradient attains its maximum value. Thus

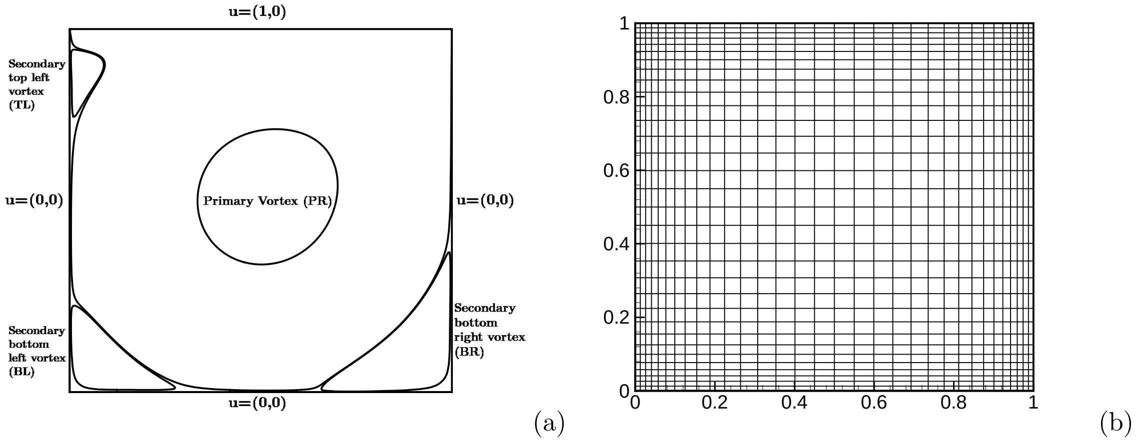

Fig. 3.7: Problem 4: (a) Schematic of lid-driven square cavity problem, (b) typical 33×33 nonuniform centrosymmetric grid.

Table 3.5: Problem 4: L_1 and L_2-norm difference in streamfunction and perceived order of convergence in space.

Re	Grid size	L_1-norm	order	L_2-norm	order
1000	65^2				
		$\lVert\psi_2 - \psi_1\rVert$=6.863399e-5		$\lVert\psi_2 - \psi_1\rVert$=9.472646e-5	
	97^2		2.04		2.04
		$\lVert\psi_3 - \psi_1\rVert$=9.225948e-5		$\lVert\psi_3 - \psi_1\rVert$=1.274255e-4	
	129^2				
3200	65^2				
		$\lVert\psi_2 - \psi_1\rVert$=1.192368e-4		$\lVert\psi_2 - \psi_1\rVert$=1.728218e-4	
	97^2		1.51		1.62
		$\lVert\psi_3 - \psi_1\rVert$=1.690068e-4		$\lVert\psi_3 - \psi_1\rVert$=2.422027e-4	
	129^2				

the maximum number of grid points are accumulated near the boundaries. This is achieved by replacing the clustering parameter in equation (2.28) with a scattering parameter. Other parameters are set to $L_x = L_y = 1$, $\Theta_x = \Theta_y = 2\pi$ in conformity with the geometry of the flow. A prototype grid is shown in Fig. 3.7b.

Analyzing the spatial order of accuracy as the steady state is approached for this problem may be interesting. Since this problem lacks an analytical solution, one must strive to achieve the perceived order of convergence (σ). Despite our best

Table 3.6: Problem 4: L_1 and L_2-norm difference in vorticity and perceived order of convergence in space.

Re	Grid size	L_1-norm	order	L_2-norm	order
1000	65^2				
		$\|\omega_2-\omega_1\|$=5.085584e-3		$\|\omega_2-\omega_1\|$=8.105967e-3	
	97^2		1.98		1.95
		$\|\omega_3-\omega_1\|$=6.874297e-3		$\|\omega_3-\omega_1\|$=1.100181e-2	
	129^2				
3200	65^2				
		$\|\omega_2-\omega_1\|$=1.568696e-2		$\|\omega_2-\omega_1\|$=2.479823e-2	
	97^2		1.64		1.85
		$\|\omega_3-\omega_1\|$=2.192499e-2		$\|\omega_3-\omega_1\|$=3.396542e-2	
	129^2				

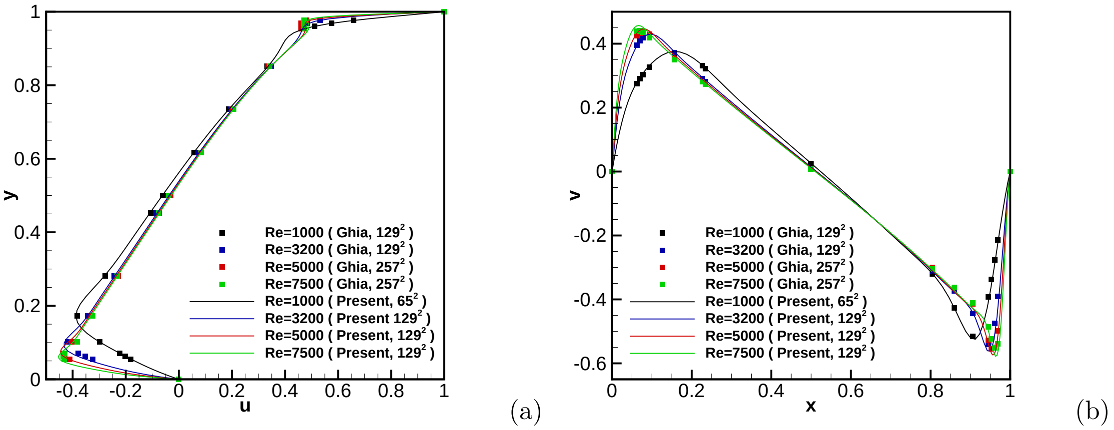

Fig. 3.8: Problem 4: Comparisons of steady-state velocities (a) u along the vertical centreline and (b) v along the horizontal centre line with [52] for $Re = 1000$, 3200, 5000 and 7500.

efforts, we were only able to trace an estimate of perceived order on a uniform grid [134]. Here, we adopt this philosophy for a nonuniform grid. At an arbitrary point P in the solution domain, let $\phi^{(P)}$ be some exact solution of this problem. We assume that the solution domain is discretized by three different nonuniform grids, $(N_1+1)\times(N_1+1)$, $(N_2+1)\times(N_2+1)$ and $(N_3+1)\times(N_3+1)$, of similar nature where the successive grids are finer compared to the previous one and are assumed

Table 3.7: Problem 4: Strength and position of the centre of primary vortex for different Reynolds numbers.

Re		Grid Size	ψ_{min}	x	y
1000	[52]	129^2	-0.118	0.5313	0.5625
	[63]	256^2	-0.118	0.5333	0.5647
	[54]	81^2	-0.117	0.5250	0.5625
	[14]	1025^2	-0.119	0.5312	0.5655
	[86]	321^2	-0.118	0.5311	0.5681
	Present	65^2	-0.118	0.5250	0.5746
2000	[163]	321^2	-0.112	0.5250	0.5500
	[63]	256^2	-0.120	0.5255	0.5490
	[54]	81^2	-0.120	0.5186	0.5496
	[86]	321^2	-0.128	0.5311	0.5681
	Present	65^2	-0.120	0.5250	0.5498
3200	[52]	129^2	-0.120	0.5165	0.5469
	[54]	161^2	-0.122	0.5188	0.5438
	[130]	129^2	-0.121	0.5156	0.5391
	[86]	321^2	-0.122	0.5186	0.5434
	Present	65^2	-0.121	0.5250	0.5498
5000	[52]	257^2	-0.119	0.5117	0.5352
	[63]	256^2	-0.121	0.5176	0.5373
	[54]	161^2	-0.122	0.5125	0.5375
	[14]	2049^2	-0.122	0.5146	0.5352
	[173]	2049^2	-0.122		
	[86]	321^2	-0.122	0.5124	0.5373
	Present	129^2	-0.122	0.5125	0.5375
7500	[52]	257^2	-0.120	0.5117	0.5322
	[63]	256^2	-0.122	0.5176	0.5333
	[54]	161^2	-0.122	0.5125	0.5313
	[86]	321^2	-0.122	0.5124	0.5311
	[173]	2049^2	-0.122		
	Present	129^2	-0.122	0.5125	0.5375

Table 3.8: Problem 4: Strength and position of the centre of secondary bottom vortices for different Reynolds numbers.

			Bottom Right			Bottom Left		
Re		Grid Size	ψ_{max}	x	y	ψ_{max}	x	y
1000	[52]	129^2	1.75e-3	0.8594	0.1094	2.31e-4	0.0859	0.0781
	[63]	256^2	1.69e-3	0.8667	0.1137	2.22e-4	0.0902	0.0784
	[54]	81^2	1.70e-3	0.8625	0.1125	2.023-4	0.0875	0.0750
	[14]	1025^2	1.73e-3	0.8633	0.1123			
	[86]	321^2	1.73e-3	0.8657	0.1123	2.32e-4	0.0833	0.0775
	Present	65^2	1.75e-3	0.8607	0.1117	2.34e-4	0.0877	0.0769
2000	[163]	321^2	2.60e-3	0.8375	0.0938	6.90e-4	0.0875	0.1063
	[63]	256^2	2.44e-3	0.8471	0.0980	7.26e-4	0.0902	0.1059
	[54]	81^2	2.41e-3	0.8375	0.1000	8.58e-4	0.0875	0.1000
	[86]	321^2	2.45e-3	0.8416	0.0956	7.17e-4	0.0863	0.1020
	Present	65^2	2.52e-3	0.8455	0.0993	7.46e-4	0.0877	0.0993
3200	[52]	129^2	3.14e-3	0.8125	0.0859	9.78e-4	0.0859	0.1094
	[54]	161^2	2.86e-3	0.8125	0.0875	1.03e-3	0.0813	0.1188
	[130]	129^2	2.93e-3	0.8203	0.0859	1.13e-3	0.0804	0.1203
	[86]	321^2	2.82e-3	0.8243	0.0833	1.11e-3	0.0804	0.1194
	Present	65^2	2.88e-3	0.8294	0.0877	1.11e-3	0.0769	0.1251
5000	[52]	257^2	3.08e-3	0.8086	0.0742	1.36e-3	0.0703	0.1267
	[63]	256^2	3.03e-3	0.8078	0.0745	1.35e-3	0.0784	0.1373
	[54]	161^2	2.96e-3	0.8000	0.0750	1.32e-3	0.0750	0.1313
	[14]	2049^2	3.07e-3	0.8057	0.0732			
	[173]	2049^2	3.06e-3					
	[86]	321^2	3.06e-3	0.8062	0.0748	1.37e-3	0.0720	0.1381
	Present	129^2	3.01e-3	0.8036	0.0717	1.37e-3	0.0717	0.1393
7500	[52]	257^2	3.28e-3	0.7813	0.0625	1.47e-3	0.0645	0.1504
	[63]	256^2	3.20e-3	0.7922	0.0667	1.51e-3	0.0706	0.1592
	[54]	161^2	3.05e-3	0.7813	0.0625	1.60e-3	0.0688	0.1500
	[173]	2049^2	3.21e-3					
	[86]	321^2	3.21e-3	0.7872	0.0642	1.53e-3	0.0642	0.1540
	Present	129^2	3.25e-3	0.7852	0.0621	1.53e-3	0.0621	0.1545

Table 3.9: Problem 4: Strength and position of the centres of secondary top left and tertiary bottom right vortices for different Reynolds numbers.

Re		Grid size	Secondary Top Left			Tertiary Bottom Right		
			ψ_{max}	x	y	ψ_{min}	x	y
2000	[54]	81^2	1.22e-4	0.0375	0.8875			
	Present	65^2	1.31e-4	0.0331	0.8749			
3200	[52]	129^2	7.28e-4	0.0547	0.8984			
	[54]	81^2	7.33e-4	0.0563	0.9000			
	[130]	129^2	8.10e-4	0.0549	0.8984			
	Present	65^2	7.69e-4	0.0575	0.9007			
5000	[52]	257^2	1.46e-3	0.0625	0.9102	-1.43e-6	0.9805	0.0195
	[63]	256^2	1.40e-3	0.0667	0.9059			
	[130]	129^2	1.60e-3	0.0625	0.9062			
	[54]	161^2	1.54e-3	0.0688	0.9125	-1.70e-6	0.9750	0.0188
	[86]	321^2				-1.38e-6	0.9787	0.0188
	Present	129^2	1.47e-3	0.0621	0.9123	-1.99e-6	0.9870	0.0175
7500	[52]	257^2	2.05e-3	0.0664	0.9141	-3.28e-5	0.9492	0.0430
	[63]	256^2	2.06e-3	0.0706	0.9098			
	[130]	129^2	2.36e-3	0.0703	0.9063			
	[54]	161^2	2.07e-3	0.0688	0.9125	-1.89e-5	0.9500	0.0375
	[86]	321^2				-3.15e-6	0.9520	0.0419
	Present	129^2	2.18e-3	0.0668	0.9123	-3.60e-5	0.9512	0.0447

to be in the ratio $1/k_1 : 1/k_2 : 1$. The computed solutions thus obtained at point P are assumed to be $\phi_1^{(P)}$, $\phi_2^{(P)}$ and $\phi_3^{(P)}$ respectively. Then

$$\phi^{(P)} - \phi_1^{(P)} \doteq C^{(P)} \left(k_1 h\right)^{\sigma}, \tag{3.26a}$$

$$\phi^{(P)} - \phi_2^{(P)} \doteq C^{(P)} \left(k_2 h\right)^{\sigma}, \tag{3.26b}$$

$$\phi^{(P)} - \phi_3^{(P)} \doteq C^{(P)} \left(h\right)^{\sigma} \tag{3.26c}$$

where $C^{(P)}$ is some constant. Eliminating $\phi^{(P)}$ and $C^{(P)}$ from the equation (3.26a) - (3.26c), we get

$$\frac{\phi_2^{(P)} - \phi_1^{(P)}}{\phi_3^{(P)} - \phi_1^{(P)}} \doteq \frac{k_1^{\sigma} - k_2^{\sigma}}{k_1^{\sigma} - 1}. \tag{3.27}$$

Finally, converting locally defined relation to a global one through the use of appropriate norm $\|.\|$, we get

$$\frac{\|\Phi_2 - \Phi_1\|}{\|\Phi_3 - \Phi_1\|} \doteq \frac{k_1^\sigma - k_2^\sigma}{k_1^\sigma - 1}. \tag{3.28}$$

This formula could be used to determine the perceived rate of convergence.

Traditionally, emphasis is to establish an order of convergence at low *Re* [86]. As low *Re* flows could be adequately resolved with coarser grids, it is easy to simulate with three increasingly finer distinct meshes necessary to estimate order. With a higher *Re* value, not only the flow complexity increases but also the coarser of the three grids should be fine enough for stable computation resolving all scales. Thus rendering the order estimation computation intensive. Further, to keep the influence of temporal truncation error at the bay, δt has to be chosen exceedingly small depending on the finest mesh size used in the process. In this connection work of Xu *et al.* [173] is commendable. The authors in their work computed using very fine meshes 513 × 513, 1025 × 1025, and 2049 × 2049 and were able to establish the order of convergence at very high Reynold numbers, $Re = 5000$ and 7500. Motivated by the work of Xu *et al.* [173] we proceed to investigate the order of convergence at $Re = 1000$ and 3200. We employ grids of sizes 65 × 65, 97 × 97 and 129 × 129 and compute with $\delta t = 1.0e - 4$ to minimize temporal error. The perceived order of convergence of streamfunction is estimated in Table 3.5 whereas convergence for vorticity is shown in Table 3.6. From these tables, it is clear that the order of convergence drops below quadratic because of increased flow complexity. We are partially constrained to investigate convergence with higher *Re* because of our modest computing resources. Nevertheless, it is amply clear that the mesh 129 × 129 should be ideally suited to compute in conjunction with our newly developed discretization strategy.

The next set of computations uses a 129×129 grid with a time step of $\delta t = 5.0e{-}3$ for *Re* up to 8050. We report steady-state results *viz.* strengths and positions of the primary, secondary and tertiary vortices in Tables 3.7 to 3.9 respectively for $Re = 1000$, 2000, 3200, 5000 and 7500. A good analogy could be established on comparison with fine mesh results available in the literature. Here, comparisons are carried out with as many as eight different works [14, 52, 54, 63, 86, 130, 163, 173] some of which [14, 173] use grid as fine as 2049. It is encouraging to note that our computation not only compare well with fine mesh computations but also is able to capture tertiary vortices using a coarser 129 × 129 grid.

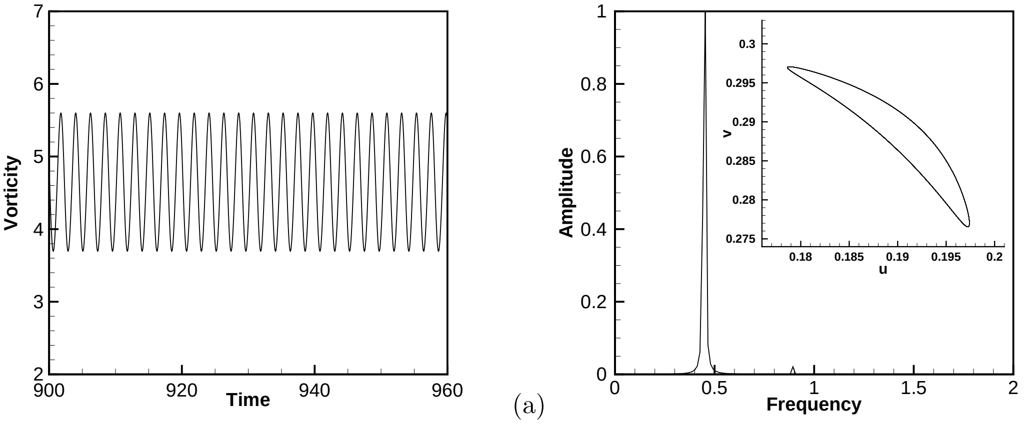

(a) (b)

Fig. 3.9: Problem 4: (a) Time history of vorticity ω and (b) power spectrum of u and v with phase portrait of u vs v (inset) for $Re = 8050$.

The values of u along the vertical centerline and v along the horizontal centerline are shown in the Fig. 3.8. Comparisons with the benchmark results of Ghia *et al.* [52] are provided as well in these figures. Although the current scheme uses a lesser number of grids, the results obtained show excellent closeness with those of [52].

High accuracy computation carried out by Bruneau and Saad [14] using uniform grid of size 513×513 and beyond reveals that "the first Hopf bifurcation takes place between $Re = 8000$ and $Re = 8050$ with less than 1% of error". Thus beyond this range, any stable discretization of the N-S system must report periodic solutions for the 2D lid-driven cavity problem. This motivates us to work with $Re = 8050$. Computation done using 129 × 129 grids indeed reports periodic state at this Re. For this problem, initialization is carried out with the steady-state solution obtained using $Re = 7500$. As reported in [14], we also notice a slow convergence towards a stable periodic solution for $Re = 8050$. Time evolution of flow fields at a monitoring point in the vicinity of $(2/16, 13/16)$ helps establish the periodic nature of the flow. We present temporal progression of vorticity at the monitoring point in Fig. 3.9a which reveals its sinusoidal variation. Spectral density analysis of the velocity com-

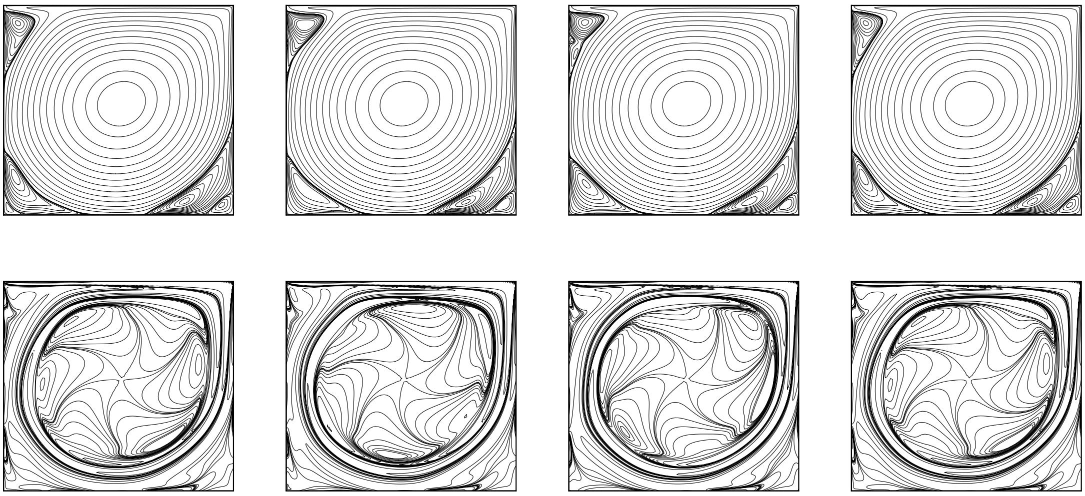

Fig. 3.10: Problem 4: Time evolution of streamfunction and vorticity in one full cycle for $Re = 8050$ on a 129×129 grid at $t = t_0$, $t = t_0 + T/3$, $t = t_0 + 2T/3$ and $t = t_0 + T$ from left to right.

ponents, presented in Fig. 3.9b, helps us ascertain periodicity of the flow with period $T = 2.22$ approximately which co-relates directly to the frequency 0.45 as reported by Bruneau and Saad [14]. To probe further we draw a phase portrait of velocity components in Fig. 3.9b (inset). In Fig. 3.10, we display the instantaneous streamfunction and vorticity contours at four different stages of one full cycle separated by $T/3$. A strong similarity can be noticed between the streamfunction contours and vorticity contours at time $t = t_0$ and $t = t_0 + T$ thereby revealing the periodic nature of the solution. To the best of our knowledge, numerical simulation of lid-driven cavity flow beyond the first Hopf bifurcation point has not been correctly captured by any discretization at such a coarser grid.

3.4.5 Problem 5: Flow past square cylinder

Investigation of the periodic vortex shedding behind bluff bodies exposed to uniform flow has fascinated researchers for a long time. This is a challenging problem in fluid mechanics involving the interaction of three shear layers: a boundary layer, a separating free shear layer, and a wake, each with different or coupled processes of resulting instabilities as the Re value is increased. An overwhelming number of studies are found on flow past bluff bodies which especially deals with circular geometries. Contrary to the extensive literature on flow past a circular cylinders, the analogous case of the square cylinder has attracted limited attention [1, 11, 13, 35, 36, 114, 133, 138, 146]. Nevertheless, it is well documented in the literature that accurate simulation around bluff bodies requires body fitted orthogonal grids with clustering on the surface. In the context of finite difference approximation, it entails coordinate transformation to generate a grid around circular as well as square cylinder. Our formulation alleviates such requirement and as discussed earlier should be free from destabilizing effects as noted elsewhere [186]. To the best of our knowledge, high order transformation-free finite difference computation of flow past square cylinder is not available in the literature. In this study, we cluster grids on the surface of the cylinder and simulate using the compact discretization hitherto developed.

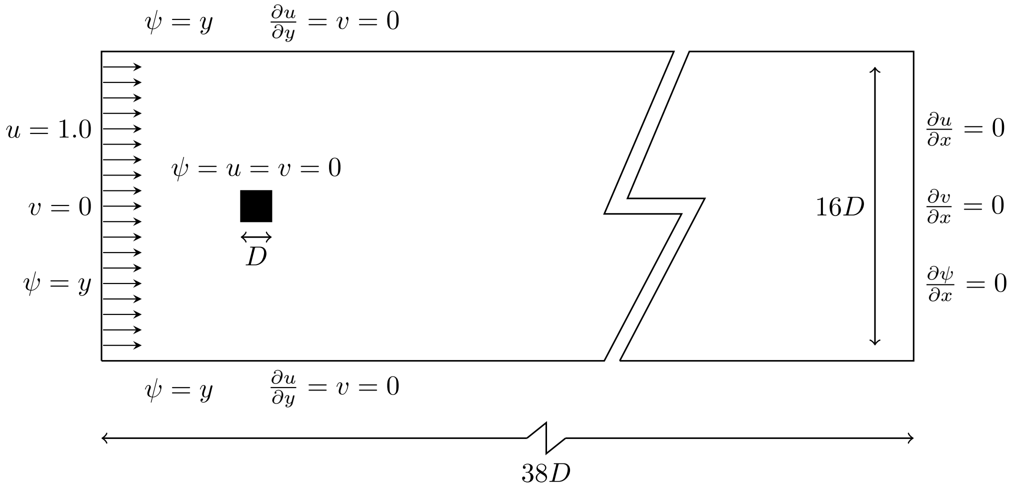

Fig. 3.11: Problem 5: Schematic diagram of the configuration for flow past a square cylinder problem.

A schematic diagram of the flow configuration is given in Fig. 3.11. A 2D square cylinder with side $D = 1$ is exposed to a constant freestream velocity U_∞. The cylinder is fixed in the Cartesian plane such that its center coincides with the origin. Top and bottom freestream are set to be equidistant from the center of the cylinder with the distance between them kept fixed at $H = 16D$. This produces a blockage $B = 0.0625$. Distances of upstream and downstream boundaries from the center

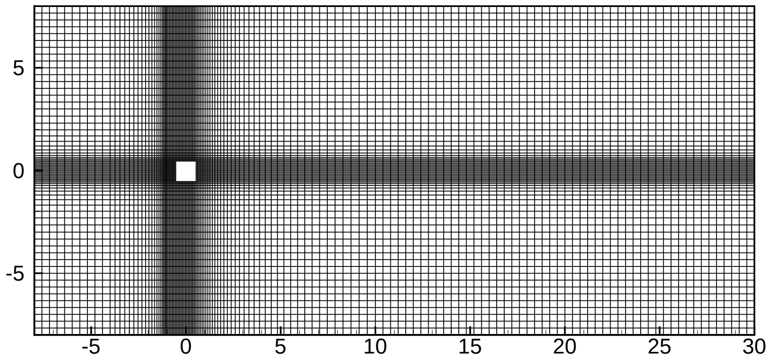

Fig. 3.12: Problem 5: Nonuniform grid generated using trigonomertic stretching functions.

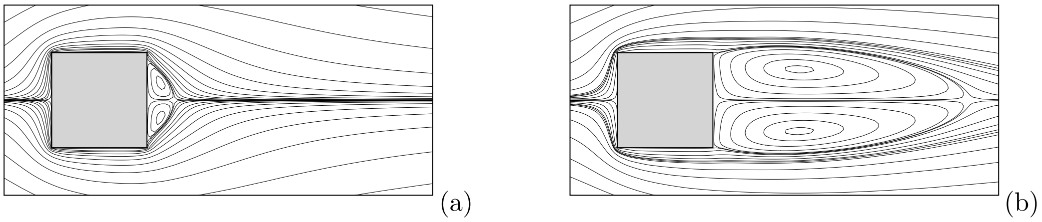

Fig. 3.13: Problem 5: Streamline plots at the steady state: (a) $Re = 5$, (b) $Re = 40$.

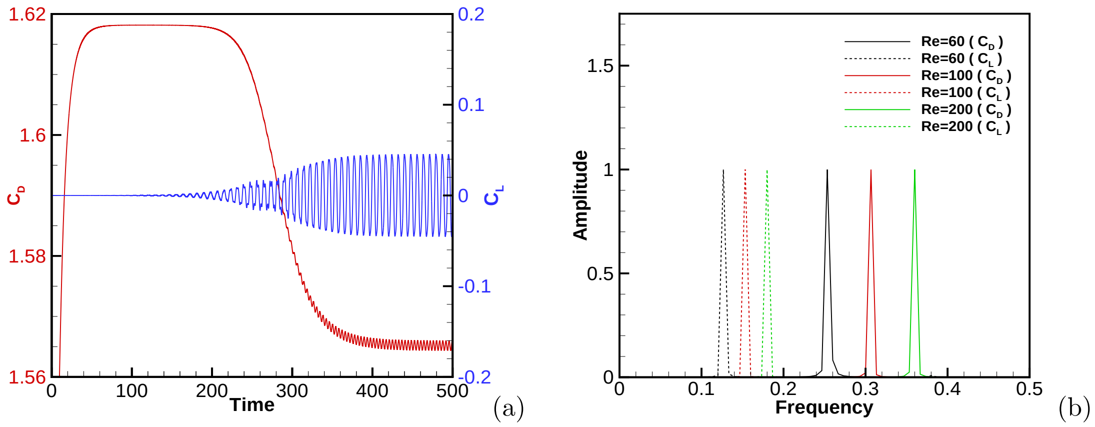

Fig. 3.14: Problem 5: (a) Time history of C_D and C_L for $Re = 60$, (b) power spectra of C_D and C_L for different Reynolds numbers.

of the cylinder are considered to be $L_u = 8D$ and $L_d = 30D$ respectively. The Reynolds number $Re = U_\infty D/\nu$, for the flow is defined using the edge length and freestream velocity with ν being the kinematic viscosity. The boundary conditions associated with this problem are shown in the schematic diagram Fig. 3.11.

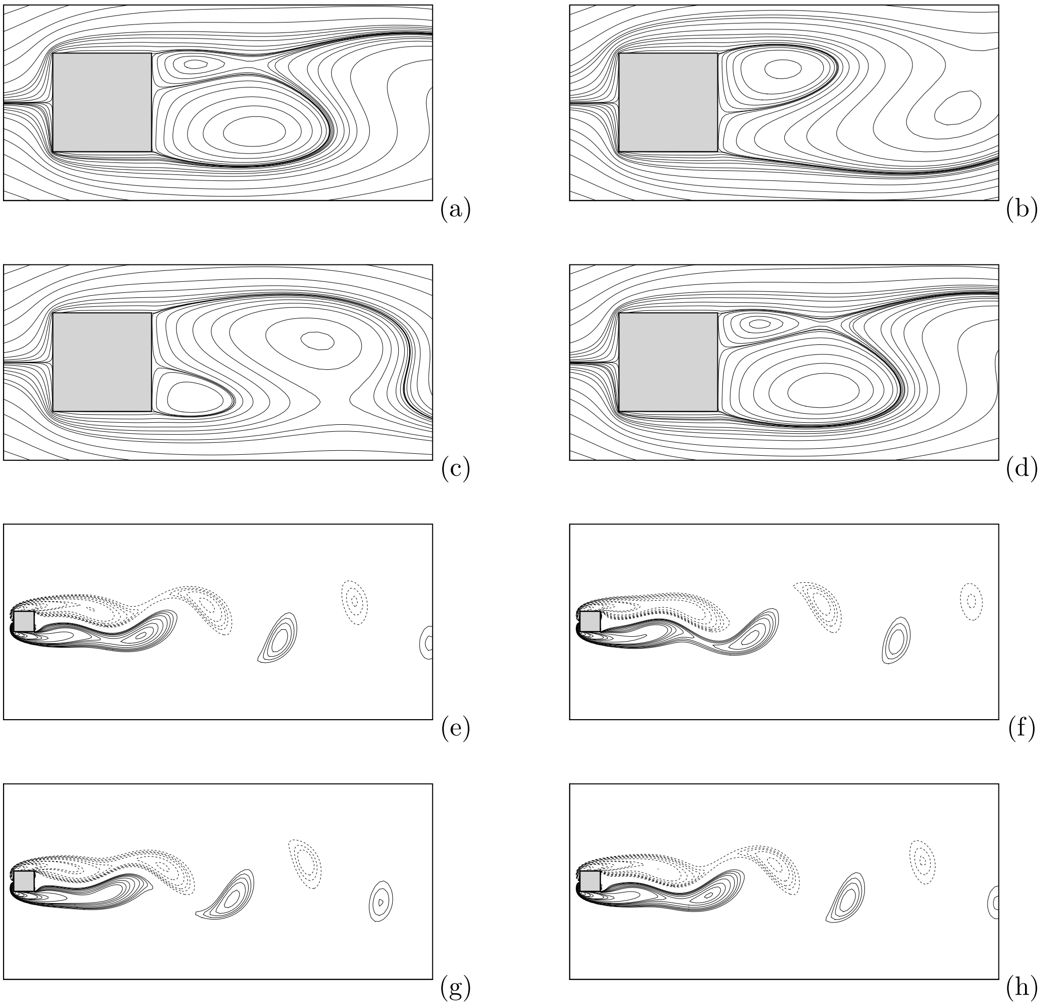

Fig. 3.15: Problem 5: (a)-(d) Streamline patterns and (e)-(h) vortex shedding for $Re = 60$ at $t = t_0$, $t = t_0 + T_{60}/3$, $t = t_0 + 2T_{60}/3$ and $t = t_0 + T_{60}$.

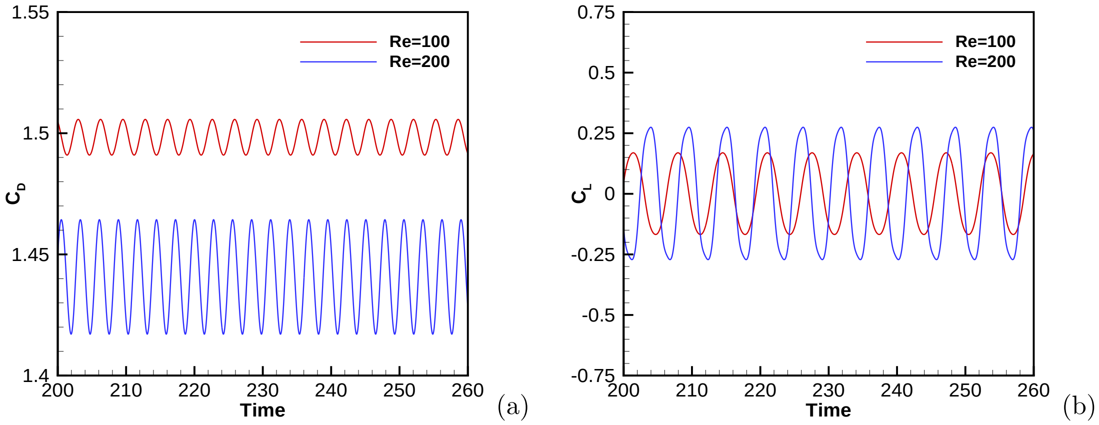

Fig. 3.16: Problem 5: Time history of (a) C_D and (b) C_L for different Reynolds numbers.

We carry out numerical simulation for as many as five different Reynolds numbers, $Re = 5$, 40, 60, 100 and 200 using $\delta t = 1.0e-2$ on a grid of size 283×141. The above choices of Reynolds number are motivated by our desire to test the efficiency of the scheme in capturing steady, transient, and periodic regimes. As documented in [13], for this problem flow remain steady with $0.5 \leq Re < 60$ and lead to unsteady flow field for $60 \leq Re \leq 300$ indicating Hopf bifurcation at around $Re = 60$. Breuer *et al.* [13] in their work has established periodic state for $Re = 60$ using a fine 561×341 grid. The same conclusion has been made by Bouaziz *et al.* [11] in their work with the help of a control volume FEM on a 249×173 nonuniform grid. The present formulation allows us to accumulate a large number of nodes in the near boundary regions of the cylinder. Thus, a nonuniform grid is laid out in the region $(x, y) \in [-4, 17] \times [-4, 4]$ as shown in Fig. 3.12. Beyond this region, a uniform grid has been used as we strive to capture the vortex shedding process with a relatively lesser number of grid points. It should be interesting to investigate near Hopf bifurcation point using a grid which is almost five times coarser than that used by Breuer *et al.* [13].

In Fig. 3.13, steady-state streamlines are displayed for $Re = 5$ and 40. In this figure, we notice the formation of a closed steady recirculating region consisting of two symmetric vortices behind the cylinder, often referred to as a separation bubble. Lengths of the separation bubbles at the steady state for both the Re's have been documented in Table 3.10. In this table, our results are compared with those of [36, 114, 133, 138]. A close resemblance with percentual error within 7% could be noticed with the standard values available in the literature pointing out the efficiency of the formulation. Note that some differences in numerical values could be ascribed to the difference in the value of the blockage ratio. In fact, our maximum difference pertains to the computation done by Dhiman *et al.* [36] in an extended computational domain with a substantially finer grid.

Next, we demonstrate our computational results for $Re = 60$, 100 and 200. Several authors [1, 11, 13] in their classical works have established a periodic state for flow past square cylinder at Re value as low as 60. It is heartening to note that we could capture the periodic state for $Re = 60$ with a nonuniform grid and much

Table 3.10: Problem 5: Comparison of Recirculation length (L/D) at steady states for different Reynolds numbers.

Re		B	L/D	%-diff.
5	[114]	0.067	0.3000	0.0
	[138]	0.050	0.3027	0.9
	[36]	0.050	0.3090	2.9
	[133]	0.067	0.3163	5.2
	Present	0.0625	0.3000	
40	[114]	0.067	2.7000	0.7
	[138]	0.050	2.8217	5.0
	[36]	0.050	2.8220	7.0
	[133]	0.067	2.7348	2.0
	Present	0.0625	2.6800	

lesser number of nodal points.

Time evolution of drag coefficient (C_D) and lift coefficient (C_L) for $Re = 60$ are displayed in Fig. 3.14, which duly indicates that our newly developed scheme has correctly captured the periodic state. To prove further spectral density analysis is carried out in Fig. 3.14b. This figure reveals time period of the flow to be $T_{60} = 7.94$ for $Re = 60$. For $Re = 60$, streamfunction and vorticity are depicted at four equal intervals of a full cycle in Fig. 3.15. The significant closeness between the streamfunction and vorticity contours at $t = t_0$ and $t = t_0 + T_{60}$ brings out the periodicity in the von Kármán vortex shedding phenomena. Near wake, transverse oscillations are visualized by streaklines obtained by time integrating path of different weightless particles released upstream of the cylinder. The computed streaklines can be found in Fig. 3.17. A close resemblance of essential features can be seen with the work of Breuer *et al.* [13].

We further compute for $Re = 100$ and 200. Time variation of C_D and C_L for $Re = 100$ and 200 at periodic state are presented in Fig. 3.16. In Fig. 3.14b spectral density analysis of $Re = 100$ and 200 can be found along with $Re = 60$. Spectral density analysis confirms a single dominant peak for both C_D and C_L for each choice of Re. We tabulate and compare estimated values of C_D and Strouhal number (St) from present work with those available in the literature in Table 3.11.

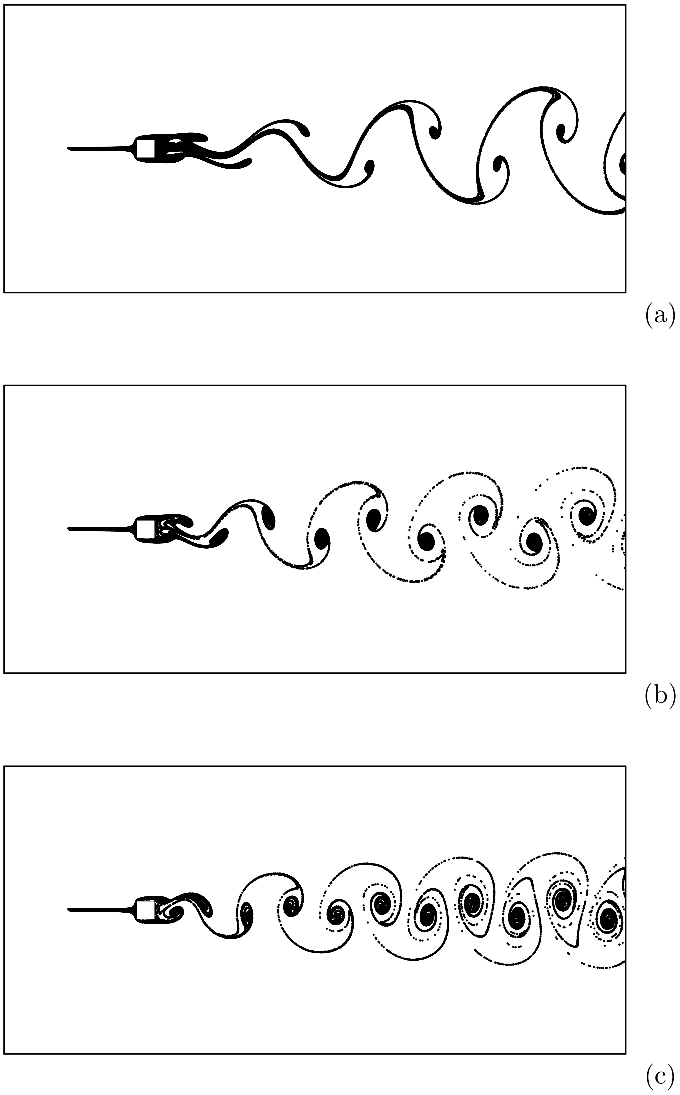

Fig. 3.17: Problem 5: Streakline patterns: (a) $Re = 60$, (b) $Re = 100$, (c) $Re = 200$.

Table 3.11: Problem 5: Comparison of flow parameters at unsteady state for different Reynolds numbers.

Re		B	C_D	%-diff.	St	%-diff.
60	[13]	0.1250	1.489	5.1	0.119	5.0
	[11]	0.1250	1.527	2.5	0.121	3.3
	[1]	0.0500	1.587	1.4	0.119	5.0
	Present	0.0625	1.565		0.125	
100	[146]	0.0250	1.444	3.7	0.144	6.3
	[146]	0.0500	1.460	2.6	0.146	4.8
	[13]	0.1250	1.356	10.5	0.138	10.9
	[11]	0.1250	1.41	6.2	0.139	10.1
	[1]	0.0500	1.47	1.9	0.141	8.5
	Present	0.0625	1.498		0.153	
200	[146]	0.0250	1.415	1.8	0.165	9.1
	[146]	0.0500	1.427	1.0	0.165	9.1
	[13]	0.1250	1.353	6.5	0.138	30.4
	[11]	0.1250	1.426	1.1	0.133	35.3
	[1]	0.0500	1.438	0.2	0.159	13.2
	Present	0.0625	1.441		0.180	

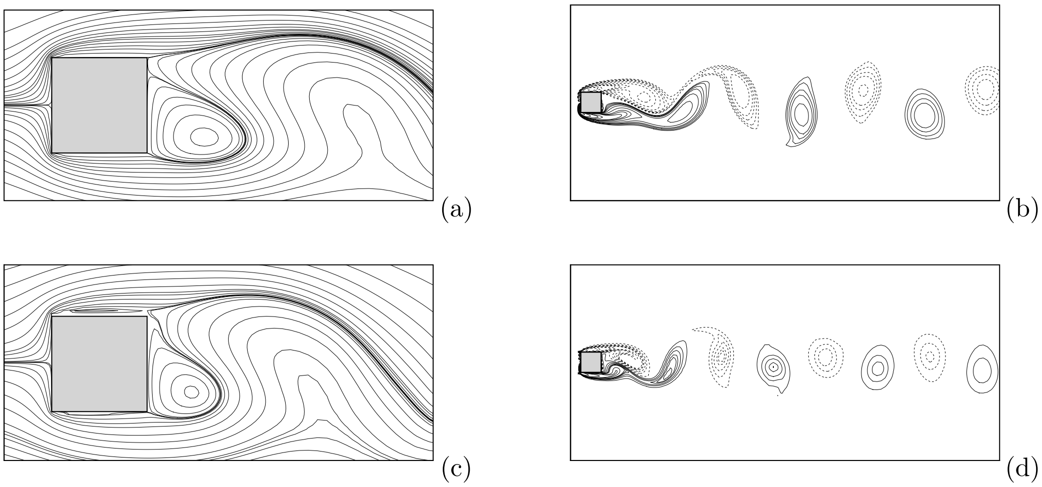

Fig. 3.18: Problem 5: Instantaneous streamfunction and vorticity contours at stable periodic stage: (a)-(b) $Re = 100$ and (c)-(d) $Re = 200$.

The relative percentual error presented in this table depicts a close match for our results. Some deviations of our flow parameters vis-à-vis the studies of Breuer *et al.* [13] and Bouaziz *et al.* [11] could be seen in Table 3.11 for higher Re values. This might be attributed to authors in [11, 13] taking recourse to parabolic velocity profile at the inlet and working with much higher blockage ratio i.e. computational domain with a smaller cross-section. Note that in our study we have introduced constant freestream at inlet following works carried out in [1, 146]. Nevertheless, our computed St number for $Re = 200$ deviate substantially. Streaklines are also computed and shown in Fig. 3.17. Further, Streamline and vorticity contours for $Re = 100$ and 200 at periodic state are given in Fig. 3.18.

3.4.6 Problem 6: Natural convection in a thermally-driven cavity

Next, we explore the diversity of our study region by entering into the heat transfer problem. In this context, we consider the 2D free heat convection inside an upright square cavity. This is known to be one of the classical problems involving heat transfer and it has been extensively studied by a number of researchers over the years [22, 27, 32, 38, 122, 157, 173, 175]. This problem finds relevance in a large number of applications in science and engineering. Here, flow is generally driven by temperature gradient and as such accurate capture of these gradients is vital. The governing equation for this problem is the transient form of the Boussinesq equation (3.19), which is written as

$$\begin{cases} \dfrac{\partial \omega}{\partial t} = -\mathbf{u} \cdot \nabla \omega + Pr \nabla^2 \omega + RaPr \dfrac{\partial \mathscr{T}}{\partial x} + f, & (3.29a) \\ \nabla^2 \psi = -\omega, & (3.29b) \\ \dfrac{\partial \mathscr{T}}{\partial t} = -\mathbf{u} \cdot \nabla \mathscr{T} + \nabla^2 \mathscr{T}. & (3.29c) \end{cases}$$

Additional temperature gradient term in equation (3.29a) gets automatically computed as the temporal advancing of temperature is carried out via equation (3.29c).

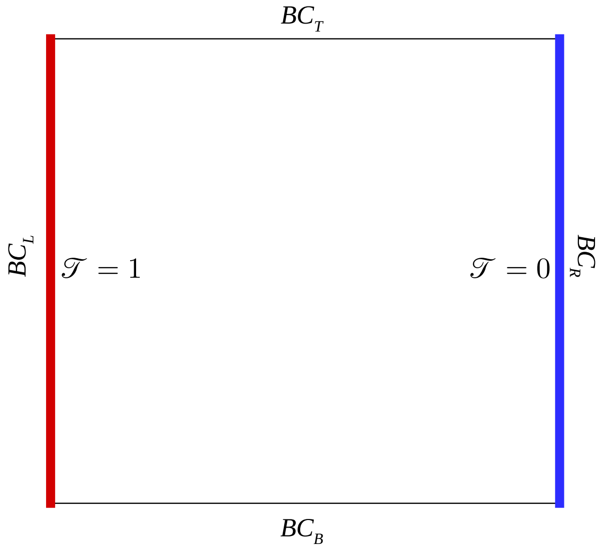

Fig. 3.19: Problem 6: Configuration of natural convection in thermally driven square cavity problem.

As seen in Fig. 3.19, two different temperatures are maintained on opposite sides of the cavity. The cavity's left wall is heated to a unit nondimensional temperature in this instance, while the right wall is maintained at zero temperature. The fluid movement inside the cavity is driven by this temperature difference. In addition to the no-slip criteria between the fluid and cavity walls, one-sided approximations introduced in the equations (3.8)–(3.11) are used to obtain the streamfunction and vorticity boundary conditions respectively. Other auxiliary conditions are delineated below:

On the left wall, BC_L: $u = v = 0, \mathscr{T} = 1$.

On the right wall, BC_R: $u = v = 0, \mathscr{T} = 0$.

On the bottom wall, BC_B: $u = v = 0, \mathscr{T}_y = 0$.

On the top wall, BC_T: $u = v = 0, \mathscr{T}_y = 0$.

The Nusselt number (Nu), which denotes the characteristics of heat transmission through the cavity, plays a very essential role in this problem. The average heat flow in the horizontal direction across any vertical line is given by

$$Nu = \int_0^1 Q(x, y)dy, \tag{3.30}$$

where, $Q(x, y)$ is the local heat flux in the x-direction at any point inside the cavity and is calculated using

$$Q(x, y) = u\mathscr{T} - \mathscr{T}_x. \tag{3.31}$$

In this work, we only stick to the Nusselt number on the hot wall along which equation (3.30) reduces to

$$Nu^0 = -\int_0^1 \mathscr{T}_x dy. \tag{3.32}$$

For efficient capture of boundary layers, a centrosymmetric nonuniform grid similar to Fig. 3.7b is generated with the stretching value $\lambda_x = \lambda_y = 0.55$ in equation (2.28). All the computations for this problem are performed while maintaining $Pr = 0.71$ fixed. For this highly coupled nonlinear problem, we simulate for larger Ra values *viz.* $Ra = 10^5$, 10^6, 10^7 and 10^8, to highlight the efficiency of the newly developed discretization. Using three different grids 65×65, 97×97 and 129×129, along with a short time step $\delta t = 1.0e - 6$, the perceived order of convergence has been investigated. The perceived order of convergence for each of the three variables, streamfunction, vorticity, and temperature, is displayed in Table 3.12. It is safe to conclude that even for the selected set of stiff flow parameters, the newly developed scheme reports an order of convergence of 1.5, despite the fact that the order of convergence appears to change for different flow variables with an increase in Ra value. We have not computed the order of convergence for $Ra = 10^8$ as such an estimate demands computations with finer grids and is avoided in this study. In

Table 3.12: Problem 6: L_2-norm difference in streamfunction, vorticity and temperature with their perceived order of convergence in space for different Rayleigh numbers.

Grid size		$Ra = 10^5$	order	$Ra = 10^6$	order	$Ra = 10^7$	order
65^2							
	$\lVert\psi_2 - \psi_1\rVert$	1.363280e-2		6.435942e-2		2.196318e-1	
97^2			1.71		1.43		1.37
	$\lVert\psi_3 - \psi_1\rVert$	1.892002e-2		9.202808e-2		3.158813e-1	
129^2							
65^2							
	$\lVert\omega_2 - \omega_1\rVert$	4.599029e0		6.857794e1		8.743296e2	
97^2			1.88		1.78		1.55
	$\lVert\omega_3 - \omega_1\rVert$	6.278344e0		9.454463e1		1.233529e3	
129^2							
65^2							
	$\lVert\mathscr{T}_2 - \mathscr{T}_1\rVert$	2.846723e-4		6.877432e-4		2.332775e-3	
97^2			1.28		1.22		1.54
	$\lVert\mathscr{T}_3 - \mathscr{T}_1\rVert$	3.948623e-4		9.681028e-4		2.986024e-3	
129^2							

Table 3.13, a quantitative comparison of the critical flow parameters computed using the proposed scheme with those available in the benchmark work by G. De Vahl Davis [27] and other stable solutions from the works [22, 32, 38, 122, 157, 173, 175] is provided. The table shows an outstanding agreement between the present data and the fine grid computations that are currently available in the literature. Note that a smaller time step, $\delta t = 5.0e-7$, was chosen for $Ra = 10^8$. Details of reference quantities considered in the table can be found in [157]. It is heartening to see that, with the possible exception of Nu^0_{max}, our computed results using a 129 × 129 grid substantially resemble those predicted using very fine mesh computations.

Fig. 3.20 presents the steady-state streamline, vorticity curves along with the isotherms for Ra ranging from 10^5 to 10^8. The contours and distributions of the present study bear an adequate closeness with similar figures presented in [22, 27, 38, 75, 122, 157, 173, 175]. From the physics of the problem, a basic conclusion can be made that for the Ra values considered in this study streamfunction, vorticity, and

Table 3.13: Problem 6: Comparison of various relevant flow parameters computed using different schemes for different Rayleigh numbers.

Ra		Grid size	$\lvert\psi_{mid}\rvert$	u_{max}	v_{max}	Nu^0	Nu^0_{max}	Nu^0_{min}
10^5	[27]	41^2	9.111	34.73	68.59	4.509	7.717	0.729
	[32]	41^2	9.1126	34.716	68.637	4.4959	7.6830	0.7279
	[157]	71^2	9.1161	34.7417	68.6383	4.5195	7.7121	0.7275
	[175]	129^2	9.1093	34.6856	68.5748	4.5226	7.7212	0.7283
	Present	129^2	9.1048	34.6835	68.4951	4.5172	7.7058	0.7279
10^6	[27]	41^2	16.320	64.63	219.36	8.817	17.925	0.989
	[157]	121^2	16.3863	64.8308	220.5676	8.8216	17.5087	0.9787
	[175]	129^2	16.3657	64.7187	220.3770	8.8235	17.5035	0.9819
	[38]	321^2	16.3409	64.4527	217.442	8.7721	17.5494	
	Present	129^2	16.3297	64.5233	219.3750	8.8015	17.4519	0.9783
10^7	[122]	129^2	29.361	148.59	699.17	16.523	39.3947	1.3664
	[157]	161^2	29.3562	148.5695	699.2991	16.5106	39.2540	1.3655
	[175]	129^2	29.3126	147.6246	696.8570	16.4890	38.7386	1.3837
	[173]	2049^2	29.3627	148.5719	699.3394	16.5241	39.4021	1.3673
	[38]	321^2	29.0604	144.406	672.739	16.2525	39.4272	
	Present	129^2	29.1048	145.9950	689.0580	16.4406	39.9850	1.3598
10^8	[122]	129^2	52.32	321.9	2222	30.225	87.24	1.919
	[22]	2043^2	52.3508	321.9063	2222.3279	30.2241	87.2454	1.9195
	[173]	2049^2	52.3265	320.9883	2223.4660	30.2265	87.4918	1.9303
	[38]	321^2	50.7929	304.344	2184.62	29.9898	87.663	
	Present	129^2	51.6680	300.3750	2113.1200	30.1655	110.3800	1.9014

temperature distribution follows a centrosymmetric nature. This is evident from Fig. 3.20. Referring to the vorticity part of Fig. 3.20a–3.20d, secondary vortices start to emerge at $Ra = 10^5$ and sustain for higher Ra values as well. Further, the vorticity contours come to the conclusion that the boundary layer thickness on both the vertical walls of the cavity progressively decreases with the increase in Rayleigh number thereby making the formation of the boundary layers more significant. Additionally, the streamfunction contour of Fig. 3.20c and 3.20d vividly

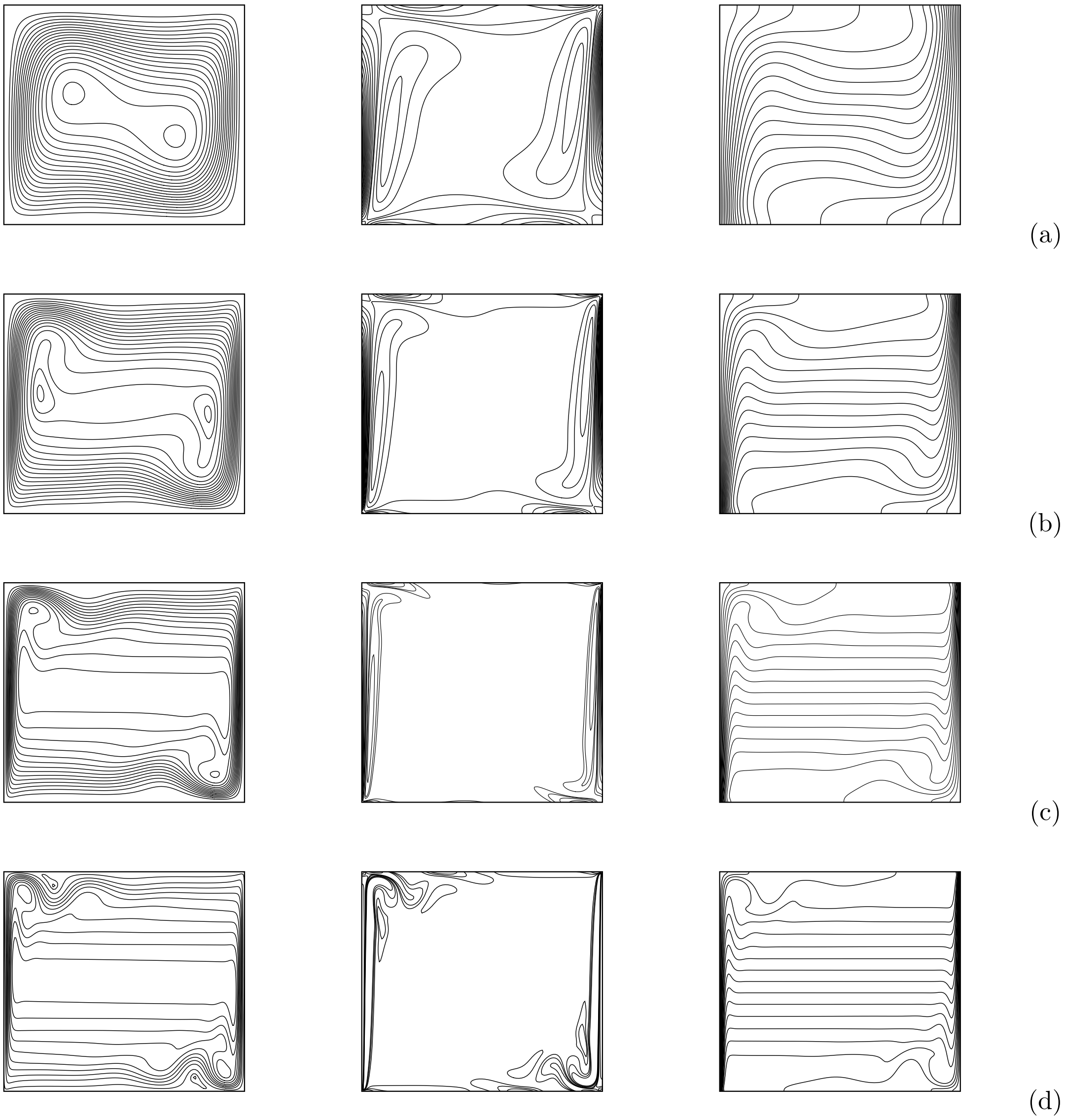

Fig. 3.20: Problem 6: Streamline (left), vorticity (middle) and temperature (right) contours at the steady state: (a) $Ra = 10^5$, (b) $Ra = 10^6$, (c) $Ra = 10^7$, (d) $Ra = 10^8$.

depicts the formation of two recirculation regions towards the top left and bottom right corners of the cavity at $Ra = 10^7$ and 10^8. These observations affirms the ones from the earlier investigations.

3.5 Conclusion

A new transformation-free compact formulation for the N-S equations has been proposed. The scheme generalizes the idea of fourth-order implicit (5,5)CC formulation to a nonuniform grid and carries a much wider appeal. Although, theoretically the scheme is only second-order accurate it is found to report higher convergence order for a linear problem with the analytical solution. This is amply clear from the application of the scheme to problems with analytical solutions. The efficiency of the scheme is earnestly documented and is found to be suitable for both primitive variable and streamfunction-vorticity formulations. Extension of one-sided approximation of first-order spatial derivative to nonuniform grid helps us tackle Neumann boundary condition with ease. The solution of two benchmark problems *viz.* lid-driven cavity and flow past square cylinder reveals the significance of the scheme in simulating accurate flow features using relatively coarser grids in almost all situations. Additionally, the scheme is used to time march to the periodic states for *Re* values near Hopf bifurcation points for both the internal cavity flow problem and the external flow past bluff body problem. It is heartening to see that the newly developed formulation uses a much coarser grid to accurately simulate flows at critical parameters. Computations carried out beyond bifurcation points bring out the versatile nature of the scheme on relatively coarser grids. Finally, the study of the natural convection problem helps establish the efficiency of the scheme for the Boussinesq equation. For lid-driven and buoyancy-driven cavity problems, we also documented the perceived order of convergence of the method.